


Article

Barotropic Instability during Eyewall Replacement

Christopher J. Slocum ^{1,*} , Richard K. Taft ², James P. Kossin ³ and Wayne H. Schubert ²

¹ NOAA Center for Satellite Applications and Research, Colorado State University, Fort Collins, CO 80523, USA

² Department of Atmospheric Science, Colorado State University, Fort Collins, CO 80523, USA

³ The Climate Service, Madison, WI 53706, USA

* Correspondence: christopher.slocum@noaa.gov

Abstract: Just before making landfall in Puerto Rico, Hurricane Maria (2017) underwent a concentric eyewall cycle in which the outer convective ring appeared robust while the inner ring first distorted into an ellipse and then disintegrated. The present work offers further support for the simple interpretation of this event in terms of the non-divergent barotropic model, which serves as the basis for a linear stability analysis and for non-linear numerical simulations. For the linear stability analysis the model's axisymmetric basic state vorticity distribution is piece-wise uniform in five regions: the eye, the inner eyewall, the moat, the outer eyewall, and the far field. The stability of such structures is investigated by solving a simple eigenvalue/eigenvector problem and, in the case of instability, the non-linear evolution into a more stable structure is simulated using the non-linear barotropic model. Three types of instability and vorticity rearrangement are identified: (1) instability across the outer ring of enhanced vorticity; (2) instability across the low vorticity moat; and (3) instability across the inner ring of enhanced vorticity. The first and third types of instability occur when the rings of enhanced vorticity are sufficiently narrow, with non-linear mixing resulting in broader and weaker vorticity rings. The second type of instability, most relevant to Hurricane Maria, occurs when the radial extent of the moat is sufficiently narrow that unstable interactions occur between the outer edge of the primary eyewall and the inner edge of the secondary eyewall. The non-linear dynamics of this type of instability distort the inner eyewall into an ellipse that splits and later recombines, resulting in a vorticity tripole. This type of instability may occur near the end of a concentric eyewall cycle.

Keywords: barotropic instability; eyewall replacement; concentric eyewalls; Hurricane Maria; linear stability analysis; non-divergent barotropic model



Citation: Slocum, C.J.; Taft, R.K.; Kossin, J.P.; Schubert, W.H. Barotropic Instability during Eyewall Replacement. *Meteorology* **2023**, *2*, 191–221. <https://doi.org/10.3390/meteorology2020013>

Academic Editors: Jimmy Dudhia and Paul D. Williams

Received: 7 January 2023

Revised: 27 February 2023

Accepted: 3 April 2023

Published: 20 April 2023



Copyright: © 2023 by the authors. Licensee MDPI, Basel, Switzerland. This article is an open access article distributed under the terms and conditions of the Creative Commons Attribution (CC BY) license (<https://creativecommons.org/licenses/by/4.0/>).

1. Introduction

The dynamical understanding of secondary eyewall formation has significantly increased in recent years through observational and theoretical analyses of well-documented cases such as Hurricanes Anita (1977), David (1979), and Allen (1980) [1], Hurricane Gilbert (1988) [2–4], Hurricane Frances (2004) [5,6], Hurricane Rita (2005) [7–11], Hurricane Wilma (2005) [12], Hurricane Gonzalo (2014) [13], and Hurricane Matthew (2016) [14]. As observational evidence has accumulated, numerical modeling efforts have proceeded at an increasing pace, using a hierarchy of models of different complexity [5,15–34]. This body of work has garnered important physical information from careful analysis of the relevant boundary layer dynamics [35–43]. This recent research on concentric eyewalls has also led to improvements in our ability to operationally forecast secondary eyewall formation and associated intensity variations [44–47].

Important observations for understanding concentric eyewall cycles were made as Hurricane Maria (2017) approached Puerto Rico from the south-east. Figure 1 shows non-operational infrared imagery from the National Oceanic and Atmospheric Administration (NOAA) Geostationary Operational Environmental Satellite 16 (GOES-16) at 03:00, 06:00, and 09:00 UTC 20 September 2017, as Hurricane Maria passed St. Croix and approached Puerto Rico, moving north-west with an estimated central surface pressure of 915 hPa and

maximum winds of 72 m s^{-1} . During the period from 05:18 to 09:50 UTC 20 September, Hurricane Maria was within range of the WSR-88D radar (TJUA), approximately 35 km south of San Juan. Figure 2 shows a sequence of radar reflectivity images from this period. These images consist of every other base scan (0.52° elevation angle), which means that the time between images is approximately 9.4 min. Each image is roughly 100 km by 100 km with the domain centered on the storm. Although not readily apparent from the satellite imagery shown in Figure 1, during this 4.5 h period Maria had a concentric eyewall structure as it approached Puerto Rico from the south-east at a speed of 7 m s^{-1} . In the interpretation of these radar images, it should be kept in mind that the hurricane's reflectivity is sampled at lower and lower levels as the storm approaches the radar. Since the radar is located 852 m above sea level, and since the scans were performed at an elevation angle of 0.52° , the WSR-88D range–height equation indicates that the storm is sampled at a height near $h(R) = 0.852 \text{ km} + R \sin(0.52^\circ) + R^2 / (2.42 a)$, where 2.42 is twice the refractive index, a is the Earth's radius in km, and the slant range R is given in km (Ref. [48], Chapter 3). The slant range to the center of Maria's eye decreases from approximately 150 km at 05:00 UTC, to 100 km at 07:00 UTC, and to 50 km at 09:00 UTC. For slant ranges of $R = 150, 100, 50 \text{ km}$, the corresponding beam heights are $h = 3.67, 2.41, 1.47 \text{ km}$, so the radar sampling in Figure 2 depicts the lower tropospheric structure of the precipitation.

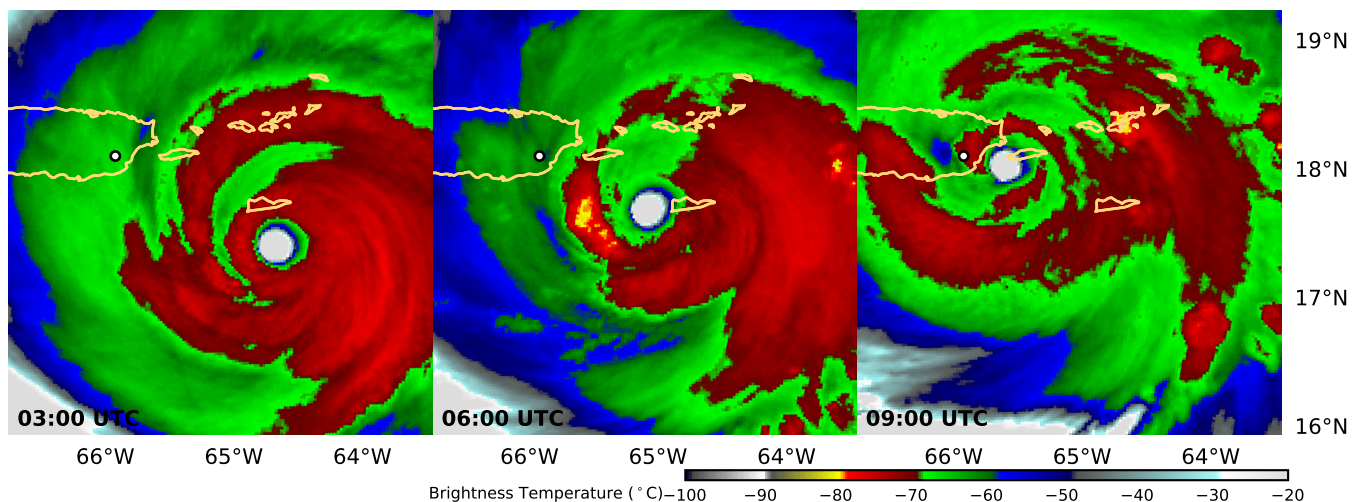


Figure 1. Color enhanced $10.3 \mu\text{m}$ infrared imagery from the NOAA GOES-16 satellite at 03:00, 06:00, and 09:00 UTC 20 September 2017. The well-defined eye of Hurricane Maria can be seen as it skirts the island of St. Croix, with a minimum sea surface pressure of approximately 915 hPa. The second and third satellite images correspond to the period of the San Juan, Puerto Rico WSR-88D radar (white dot) images shown in Figure 2 and to the aircraft traverses shown in Figures 3 and 4. Note that these satellite images reveal little evidence of the concentric eyewall structure that exists below the cirrus.

Although the end of the radar sequence shown in Figure 2 marks the destruction of the radar due to winds in excess of 65 m s^{-1} , this radar data documents an apparently important aspect of a concentric eyewall cycle—the dynamic instability and rearrangement of the potential vorticity structure associated with the inner eyewall. This behavior can be seen by noting that the concentric eyewall structure was well-defined during the period 02:00 to 05:00 UTC 20 September, when the eye was passing south of St. Croix. However, during the period 05:00 to 09:00 UTC, the inner eyewall structure distorted into a rotating ellipse that became filamented and ultimately destroyed (see Figure 2). A clearer depiction of Maria's eyewall cycle can be obtained from the animated version (which includes every base scan) of Figure 2; see the Data Availability Statement for access. Table 1 and Figure 3 summarize the tracks for five storm traverses made by an Air Force WC-130J flying at 10,000 feet ($\sim 3 \text{ km}$) during the 5.5 h period from 3:00 to 8:30 UTC 20 September. Radial

profiles of temperature, dewpoint temperature, and wind speed for these five traverses are shown in Figure 4. Traverse 4 (along the storm track) shows local wind speed maxima of 54 m s^{-1} at $r = 11 \text{ km}$ and 60 m s^{-1} at $r = 32 \text{ km}$. During the five traverses, it is also worth noting two aspects of the dewpoint temperature depression evolution. In the moat, the dewpoint temperature depression is highly variable due to the rapid rotation rate of the inner-eyewall ellipse. Initially, the dewpoint depression shows a relatively symmetric feature approximately 7–9 km wide in Traverse 3. Traverse 4, which is mostly along the minor axes of the ellipse, shows a wider region of dewpoint depression, 11–12 km. Traverse 5 enters as the major axis passes and exits along the minor axes. In the eye, the dewpoint temperature depression changes from 15°C to near zero from Traverse 1 to 4, which is indicative of a decrease in eye subsidence as a result of the weakening inner eyewall [49–51].

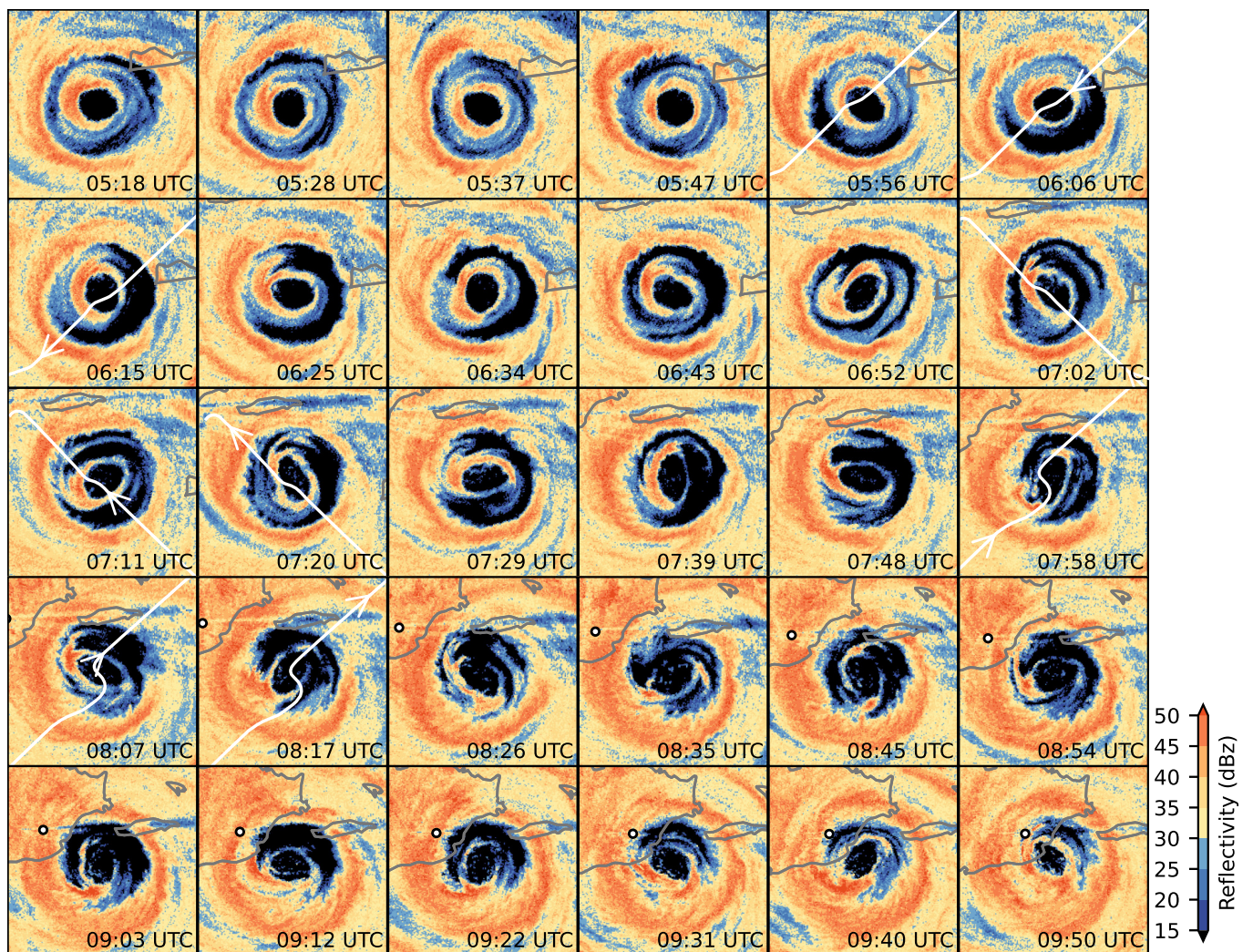


Figure 2. San Juan, Puerto Rico TJUA WSR-88D (denoted by white dot visible in the bottom two rows) images from 05:18 to 09:50 UTC 20 September 2017. Every other base scan (0.52° elevation angle) has been plotted, which means that the time between images is approximately 9.4 min. The first row shows Maria passing south-west of St. Croix, while the last row shows the storm passing south-west of Vieques and making landfall on Puerto Rico, just before destroying the radar. Each radar image is roughly 100 km by 100 km with the domain centered on the moving storm. The reflectivity scale is at the lower right, with the low reflectivity of the eye and the moat indicated in shades of blue, and the

high reflectivity of the primary and secondary eyewalls indicated in shades of orange and red. The wavenumber $m = 2$ distortion of the inner eyewall is particularly evident in several images in the second, third, and fourth rows. The white line shows the Air Force WC-130J aircraft traverses 3–5 from Table 1 and Figure 3 with the white arrow denoting the aircraft position at the time of the base scan.

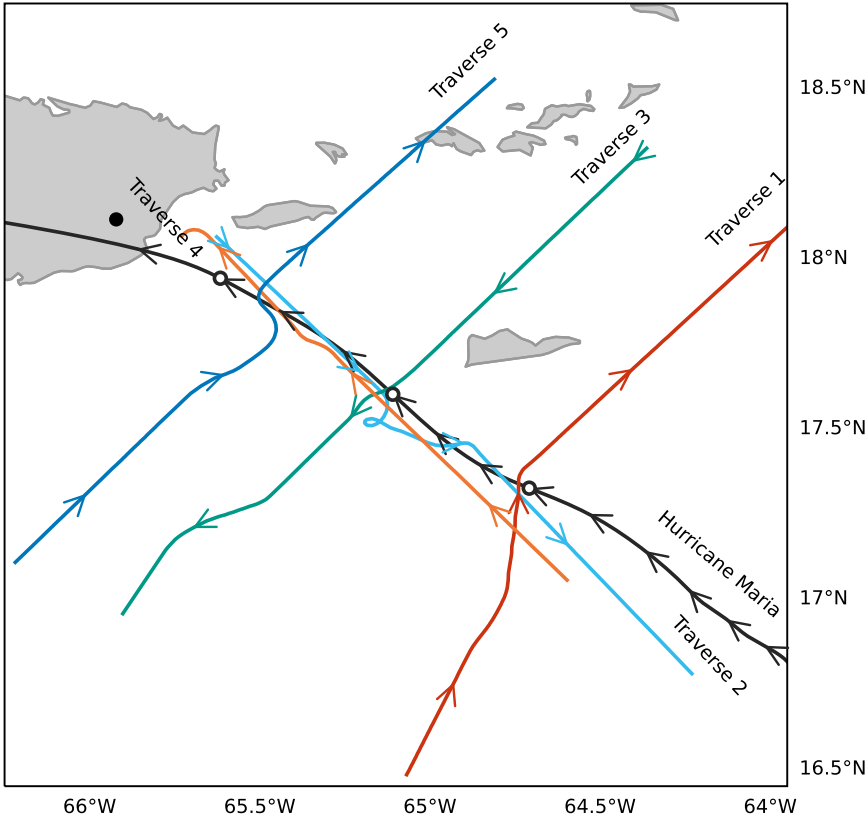


Figure 3. Aircraft tracks for five storm traverses made by the Air Force WC-130J flying at 10,000 feet (~3 km) during the 5.5 h period from 2:55 to 8:25 UTC 20 September (colored arrows at 10 min intervals denote flight direction). Table 1 contains the directions and times for the five traverses. The black curve shows Hurricane Maria’s track based on aircraft and radar center position fixes (black arrows at 1 h intervals). The three white dots along the track correspond to the satellite imagery shown in Figure 1 and the black dot is the location of the San Juan, Puerto Rico TJUA WSR-88D.

Table 1. Summary of five Air Force WC-130J aircraft traverses of Maria on 20 September 2017, with the second column showing the direction of the traverse, with the third and fourth columns showing the start and end times of the traverse to the nearest 5 min. Traverses 3–5 occurred during the radar sequence shown in Figure 2.

Traverse	Direction of Traverse	Start (UTC)	End (UTC)
1	SW to NE (perpendicular to track)	2:55	3:30
2	NW to SE (parallel to track)	4:20	5:00
3	NE to SW (perpendicular to track)	5:50	6:25
4	SE to NW (parallel to track)	6:55	7:25
5	SW to NE (perpendicular to track)	7:45	8:25

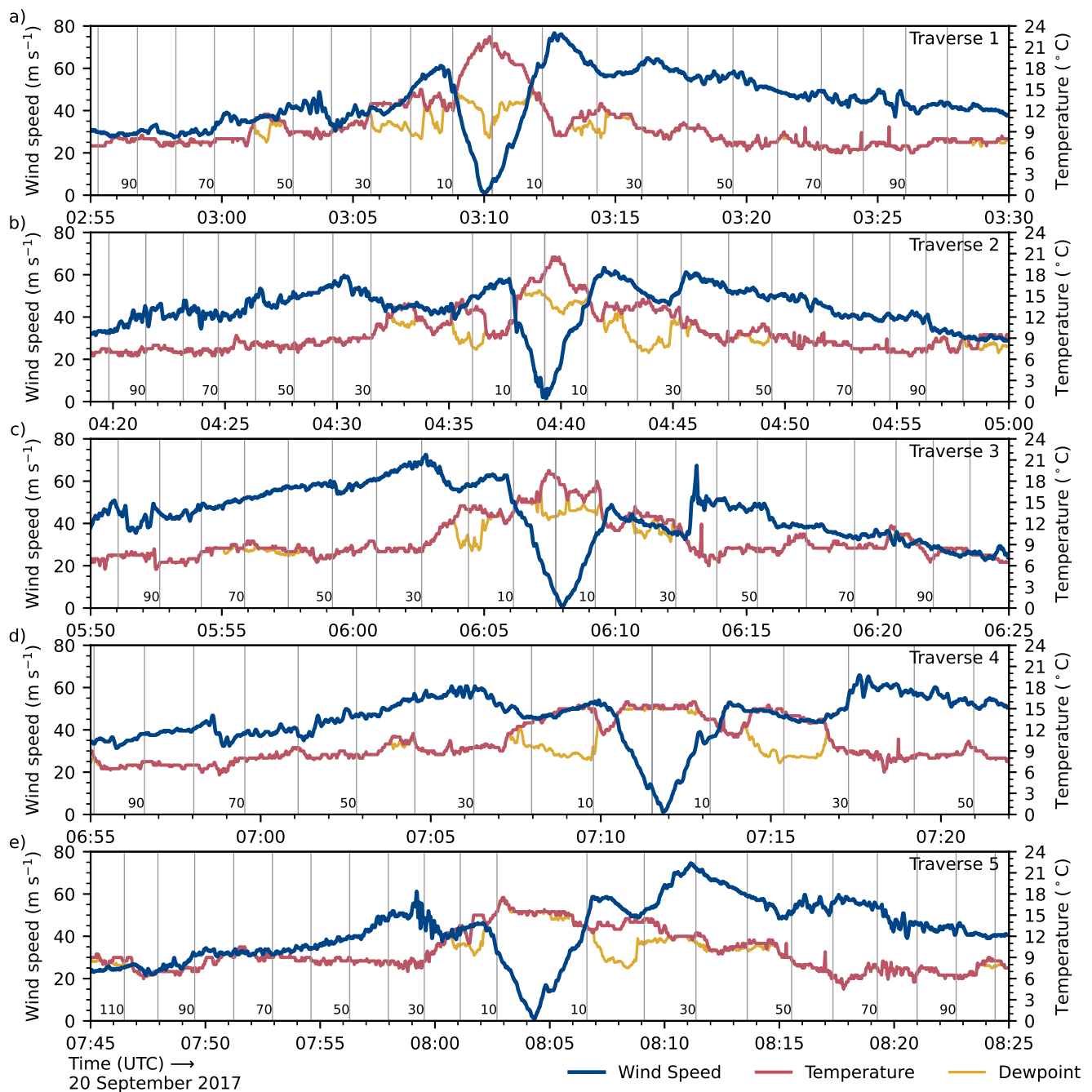


Figure 4. Traverse time series of wind speed (m s^{-1} , blue curves), temperature ($^{\circ}\text{C}$, red curves), and dewpoint temperature ($^{\circ}\text{C}$, yellow curves) at 10,000 feet for the five WC-130J traverses summarized in Table 1 and shown in Figure 3. Gray vertical lines denote the distance to the center of Hurricane Maria at 10 km intervals. Since the dewpoint instrument is unreliable in heavy rain, the dewpoint reading is shown only where it does not exceed the temperature reading.

Concentric eyewall structures and associated wind speed profiles, such as those shown in Figures 2 and 4, raise questions about possible dynamic instability. The simplest arguments concerning such instability can be made with the non-divergent barotropic model. Note that we limit the focus of the present study to the barotropic aspects of the final stages of a concentric eyewall cycle. Despite the limitations of the non-divergent barotropic model to observed tropical cyclones, the results in prior theoretical work using the non-divergent barotropic model have offered insight into observed features [52,53]. This suggests that providing a more generalized version of the analysis in Kossin et al. [53]—as

done in Lai et al. [34] for full-physics models—might provide insight into the observations collected during Hurricane Maria. It is important to note however that many aspects of the problem cannot be explained by such a simple model, including the important effect of environmental vertical wind shear [54–58], which complicates the whole process, as discussed by Didlake et al. [13] for Hurricane Gonzalo (2014), by Dougherty et al. [59] for Hurricane Bonnie (1998), and by Cha and Bell [14] for Hurricane Matthew (2016). In the non-divergent barotropic model, a Hurricane Maria-like vortex can be idealized (see Figure 5) as an axisymmetric flow field with five distinct regions of vorticity: an eye region ($0 \leq r < r_1$) of moderate vorticity; an inner eyewall region ($r_1 < r < r_2$) of high vorticity; a moat region ($r_2 < r < r_3$) of relatively low vorticity; an outer eyewall region ($r_3 < r < r_4$) of high vorticity; and a far field region ($r_4 < r < \infty$) of irrotational flow. For this five-region (four-interface) model, the three simplest types of instability are as follows: instability across the outer eyewall, in which the vorticity waves at r_3 and r_4 interact through phase locking and mutual growth; instability across the moat, in which the vorticity waves at r_2 and r_3 interact; and instability across the inner eyewall, in which the vorticity waves at r_1 and r_2 interact. Instability across the inner eyewall was studied by Schubert et al. [52] and Hendricks et al. [60] using a three-region (two-interface) model, with the goal of understanding polygonal eyewalls and inner core vorticity mixing. Instability across a concentric eyewall and across the moat was studied by Kossin et al. [53] using a four-region (three-interface) model in which the inner vorticity structure was not hollow, so that there existed only instability across the outer eyewall and across the moat. Kossin et al. [53] showed that instability across the outer eyewall occurs when the outer vorticity ring is sufficiently narrow and when the circulation of the central vortex is sufficiently weak that it does not induce enough differential rotation across the outer ring to stabilize it. Instability across the moat occurs when the radial extent of the moat is sufficiently narrow to permit phase locking and mutual growth. In one of the non-linear numerical model simulations of Kossin et al. (see their Figure 13), instability across the moat led to filamentation and mixing of the outer vorticity ring while the robust inner disk of vorticity was distorted into a rotating ellipse. This numerical integration, with its high-vorticity inner core, has some resemblance to Hurricane Maria, but the radar data in Figure 2 indicates that the outer vorticity ring is more robust and the inner ring is the one that filaments and mixes.

In documenting the elliptical eyewalls in Typhoon Herb (1996), Kuo et al. [61] and Oda et al. [62] interpreted this case in terms of the classical Kirchhoff vortex solution ([63], page 232) and dynamic instability, respectively. In particular, to explain the radar observations of Typhoon Herb, Oda et al. [62] argued that the elliptical eyewall structure was likely caused by a dynamic instability arising from radial shear in the tangential flow. To further examine this possibility, a linear eigenvalue problem was set up using the asymmetric balance model [64], with the basic flow patterned after the Typhoon Herb surface winds during the time it had concentric eyewalls. The results showed that an unstable mode appears with an azimuthal wavenumber of two. The eigenmode structure and rotation period of this unstable perturbation were comparable with the Typhoon Herb observations. These results suggest that barotropic instability due to the radial shear of tangential flow was relevant to the formation of the elliptical eye in Typhoon Herb. The barotropic instability results presented here are consistent with those of Oda et al. [62], although the dynamical model used here is simpler since it has no vertical structure.

In a recent study, Lai et al. [34] have analyzed an interesting weather research and forecasting (WRF) model simulation of a concentric eyewall cycle in Hurricane Wilma. In order to better understand the dynamic processes occurring in this full-physics model simulation, they also performed a linear stability analysis and non-linear simulations using a non-divergent barotropic model. Their results show the importance of wavenumber-two barotropic instability across the moat in diluting the vorticity of the inner eyewall of Hurricane Wilma. To further explain the dynamics of instability across the moat, Lai et al. [65–67] conducted numerical experiments with a hierarchy of models, including the full-physics WRF model. Two simulations with the three-dimensional, non-hydrostatic, 1 km resolution,

doubly nested, WRF model were made. The first experiment was with full physics, i.e., with WRF moist physics, radiative heating and cooling, and a frictional boundary layer. In the second experiment, all these physical processes were disabled, so that dynamical instability in its pure inviscid, adiabatic form could be simulated. The two experiments were initialized with a double-eyewall structure, and both evolved with a wavenumber-two barotropic instability across the moat. However, there were considerable differences in their azimuthal mean, absolute angular momentum budgets because the full-physics experiment contained a fundamental aspect of the circulation that was missing in the second experiment—a secondary circulation forced by diabatic and frictional processes.

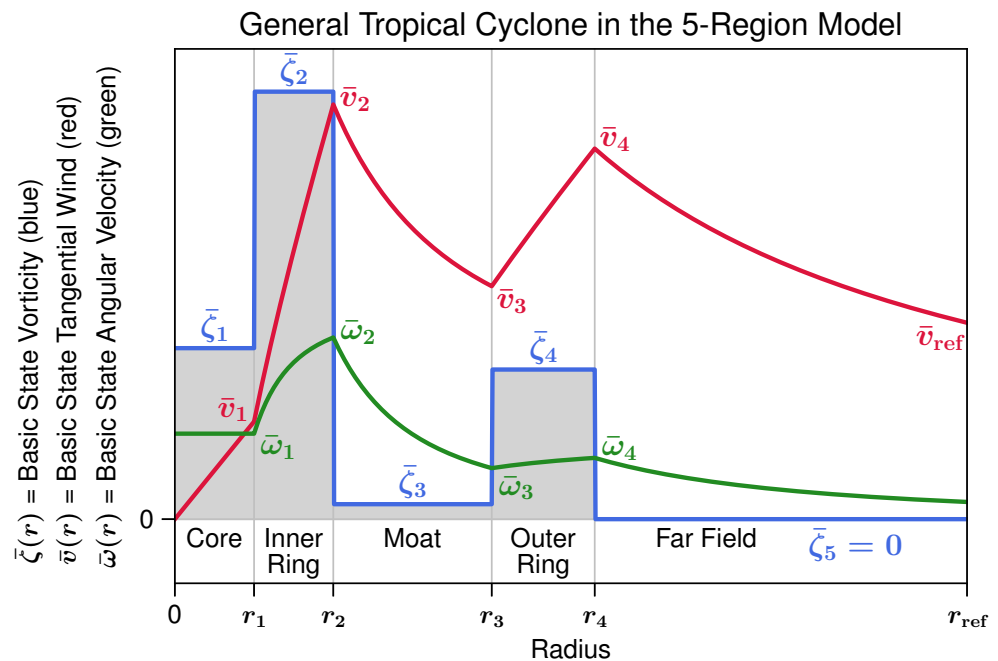


Figure 5. Axisymmetric basic state vortex for the linear stability analysis. The specified geometrical parameters are r_1, r_2, r_3 , and r_4 , and the specified vorticity parameters are $\bar{\zeta}_1, \bar{\zeta}_2, \bar{\zeta}_3$, and $\bar{\zeta}_4$, resulting in the basic state tangential wind $\bar{v}(r)$ (red) and the basic state angular velocity $\bar{\omega}(r)$ (green). The initial condition in (30) for the non-linear numerical model is identical to this figure except that the vorticity discontinuities and the kinks in tangential wind and angular velocity are smoothed over by a small radial interval. All the stability calculations presented here use $r_{ref} = 100$ km and $\bar{v}_{ref} = 20 \text{ m s}^{-1}$, so that the family of basic state vortices has a fixed “synoptic-scale environment” but each member has a different “mesoscale distribution” of vorticity inside $r = 100$ km.

The present work focuses on a barotropic interpretation of the Hurricane Maria observations, thereby extending the analyses of Kossin et al. [53], Slocum et al. [68], Taft et al. [69], Lai et al. [34,65–67], and Rostami and Zeitlin [70], and further exploring possible instabilities that may occur after the formation of a concentric eyewall structure, if the moat between the two eyewalls is sufficiently narrow. In our analysis we shall make use of a five-region, linearized barotropic model and then perform non-linear numerical integrations that illustrate how instability across the moat could have led to the disintegration of the inner vorticity ring of Hurricane Maria. The emphasis of the present linear analysis is on the structure of the eigenfunctions and on the active regions of transformation of basic state kinetic energy to eddy kinetic energy. The results of the linear analysis for a family of idealized vortices are given in Section 2 with the energetics of the linear dynamics in Section 2.3. We then explore this family of idealized vortices with the non-linear barotropic model integrations of vorticity with associated energetics in Section 3.

2. Linear Stability Analysis

As a motivation and guide for the numerical experiments described in Section 3, we begin by considering the linear stability analysis of an axisymmetric basic state vortex whose angular velocity $\bar{\omega}(r)$, or tangential wind $\bar{v}(r) = r\bar{\omega}(r)$, is a given function of radius r . Using polar coordinates (r, ϕ) , assume that the small amplitude perturbations of the streamfunction, $\psi'(r, \phi, t)$, are governed by the linearized, non-divergent, barotropic vorticity equation

$$\left(\frac{\partial}{\partial t} + \bar{\omega} \frac{\partial}{\partial \phi}\right) \nabla^2 \psi' - \frac{\partial \psi'}{r \partial \phi} \frac{d\bar{\zeta}}{dr} = 0, \quad (1)$$

where $\bar{\zeta}(r) = d(r^2 \bar{\omega})/r dr$ is the basic state vorticity, $(u', v') = (-\partial \psi'/r \partial \phi, \partial \psi'/\partial r)$ the perturbation radial and tangential components of velocity, and $\partial(rv')/r \partial r - \partial u'/r \partial \phi = \nabla^2 \psi'$ the perturbation vorticity. Searching for solutions of the form $\psi'(r, \phi, t) = \hat{\psi}^{(m)}(r) e^{i(m\phi - \nu^{(m)}t)}$, where the integer m is the azimuthal wavenumber and $\nu^{(m)} = \nu_r^{(m)} + i\nu_i^{(m)}$ the complex frequency, we obtain from (1) the radial structure equation

$$\left(\bar{\omega} - \frac{\nu^{(m)}}{m}\right) \left[\frac{d}{dr} \left(r \frac{d\hat{\psi}^{(m)}}{dr} \right) - \frac{m^2}{r^2} \hat{\psi}^{(m)} \right] - \hat{\psi}^{(m)} \frac{d\bar{\zeta}}{dr} = 0. \quad (2)$$

This radial structure equation serves as the basis for the discussions in the remainder of this section.

2.1. Review of the Rayleigh and Fjörtoft Conditions

In order to better understand the possible hydrodynamic instability of concentric eyewall structures, it is useful to recall the Rayleigh and Fjörtoft necessary conditions for barotropic instability. These two conditions are easily derived by first writing (2) in the form

$$\left(\frac{\bar{\omega} - \nu^{(m)*}/m}{|\bar{\omega} - \nu^{(m)}/m|^2} \right) \hat{\psi}^{(m)} \frac{d\bar{\zeta}}{dr} - \frac{d}{dr} \left(r \frac{d\hat{\psi}^{(m)}}{dr} \right) + \frac{m^2}{r^2} \hat{\psi}^{(m)} = 0, \quad (3)$$

where the star superscript denotes complex conjugate. We assume that $\nu_i^{(m)} \neq 0$ so that (3) is non-singular within the domain. Multiply (3) by $r\hat{\psi}^{(m)*}$ and integrate over r to obtain

$$\int_0^\infty \left(\frac{\bar{\omega} - \nu^{(m)*}/m}{|\bar{\omega} - \nu^{(m)}/m|^2} \right) |\hat{\psi}^{(m)}|^2 \frac{d\bar{\zeta}}{dr} dr + \int_0^\infty \left(\left| \frac{d\hat{\psi}^{(m)}}{dr} \right|^2 + \frac{m^2}{r^2} |\hat{\psi}^{(m)}|^2 \right) r dr = 0. \quad (4)$$

From the real and imaginary parts of (4), we obtain

$$\int_0^\infty \left(\frac{\bar{\omega} - \nu_r^{(m)}/m}{|\bar{\omega} - \nu^{(m)}/m|^2} \right) |\hat{\psi}^{(m)}|^2 \frac{d\bar{\zeta}}{dr} dr + \int_0^\infty \left(\left| \frac{d\hat{\psi}^{(m)}}{dr} \right|^2 + \frac{m^2}{r^2} |\hat{\psi}^{(m)}|^2 \right) r dr = 0, \quad (5)$$

$$\nu_i^{(m)} \int_0^\infty \frac{|\hat{\psi}^{(m)}|^2}{|\bar{\omega} - \nu^{(m)}/m|^2} \frac{d\bar{\zeta}}{dr} dr = 0. \quad (6)$$

The Rayleigh necessary condition for barotropic instability follows directly from (6). Since $|\hat{\psi}^{(m)}|^2$ and $|\bar{\omega} - \nu^{(m)}/m|^2$ are non-negative and $\nu_i^{(m)} \neq 0$, a necessary condition for instability is that $d\bar{\zeta}/dr$ have both signs in the domain. This can be interpreted as allowing the existence of counter-propagating Rossby waves.

The Fjörtoft necessary condition for instability comes from combining (5) and (6). Define $\bar{\omega}_s = \bar{\omega}(r_s)$, where r_s is a point at which $d\bar{\zeta}/dr = 0$. Multiplying (6) by $\bar{\omega}_s - \nu_r^{(m)}/m$ we obtain

$$\int_0^\infty \left(\frac{\bar{\omega}_s - \nu_r^{(m)}/m}{|\bar{\omega} - \nu^{(m)}/m|^2} \right) |\hat{\psi}^{(m)}|^2 \frac{d\bar{\zeta}}{dr} dr = 0. \quad (7)$$

Subtracting (7) from (5) yields

$$\int_0^\infty \left(\frac{\bar{\omega} - \bar{\omega}_s}{|\bar{\omega} - \nu^{(m)}/m|^2} \right) |\hat{\psi}^{(m)}|^2 \frac{d\bar{\zeta}}{dr} dr + \int_0^\infty \left(\left| \frac{d\hat{\psi}^{(m)}}{dr} \right|^2 + \frac{m^2}{r^2} |\hat{\psi}^{(m)}|^2 \right) r dr = 0, \quad (8)$$

for which the second integral is always positive. Thus, for the first integral to be negative, we must have

$$(\bar{\omega} - \bar{\omega}_s) \frac{d\bar{\zeta}}{dr} < 0 \quad (9)$$

somewhere in the flow. This is the Fjørtoft necessary condition for instability, which can be interpreted as allowing the phase locking of counter-propagating Rossby waves. For example, consider the somewhat smoothed versions of the $\bar{\omega}(r)$ and $\bar{\zeta}(r)$ profiles shown in Figure 5, so that $d\bar{\zeta}/dr$ is finite for all radii and $\bar{\zeta}(r)$ is not entirely flat in the core, inner ring, moat, and outer ring. Suppose we choose r_s where $d\bar{\zeta}/dr = 0$ in the moat of this somewhat smoothed vortex. Then, $\bar{\omega} - \bar{\omega}_s > 0$ and $d\bar{\zeta}/dr < 0$ on the inside edge of the moat while $\bar{\omega} - \bar{\omega}_s < 0$ and $d\bar{\zeta}/dr > 0$ on the outside edge of the moat, so that both the Rayleigh and Fjørtoft conditions indicate the possibility of instability across the moat. In other words, the wave on the inside edge of the moat propagates clockwise (since $d\bar{\zeta}/dr < 0$ there) relative to the strong local angular velocity. In contrast, the wave on the outside edge of the moat propagates anticlockwise (since $d\bar{\zeta}/dr > 0$ there) relative to the weaker local angular velocity. This general structure of the $\bar{\omega}(r)$ and $\bar{\zeta}(r)$ profiles allows for possible phase locking and mutual amplification of the Rossby waves.

Similarly, suppose we choose r_s where $d\bar{\zeta}/dr = 0$ in the inner eyewall. Then, $\bar{\omega} - \bar{\omega}_s < 0$ and $d\bar{\zeta}/dr > 0$ on the inside edge of the inner eyewall while $\bar{\omega} - \bar{\omega}_s > 0$ and $d\bar{\zeta}/dr < 0$ on the outside edge of the inner eyewall, so that both the Rayleigh and Fjørtoft conditions indicate the possibility of instability across the inner eyewall. The argument for possible instability across the outer eyewall is identical. To summarize, concentric eyewall structures have the distinct possibility of supporting three basic patterns of barotropic instability. In order to better understand the growth rates and spatial structures of these unstable flows, Section 2.2 presents an eigenvalue/eigenfunction analysis of the five-region model of concentric eyewalls.

2.2. Five-Region Model

We now consider in more detail the five-region basic state vortex (Figure 5), which is a simple model of a concentric eyewall structure. This basic state vortex has the tangential wind and vorticity distributions given by

$$r\bar{v}(r) = \begin{cases} \frac{1}{2}\bar{\zeta}_1 r^2 & \text{if } 0 \leq r \leq r_1, \\ r_1\bar{v}_1 + \frac{1}{2}\bar{\zeta}_2(r^2 - r_1^2) & \text{if } r_1 \leq r \leq r_2, \\ r_2\bar{v}_2 + \frac{1}{2}\bar{\zeta}_3(r^2 - r_2^2) & \text{if } r_2 \leq r \leq r_3, \\ r_3\bar{v}_3 + \frac{1}{2}\bar{\zeta}_4(r^2 - r_3^2) & \text{if } r_3 \leq r \leq r_4, \\ r_4\bar{v}_4 & \text{if } r_4 \leq r < \infty, \end{cases} \quad \text{and} \quad \bar{\zeta}(r) = \begin{cases} \bar{\zeta}_1 & \text{if } 0 \leq r \leq r_1, \\ \bar{\zeta}_2 & \text{if } r_1 < r \leq r_2, \\ \bar{\zeta}_3 & \text{if } r_2 < r \leq r_3, \\ \bar{\zeta}_4 & \text{if } r_3 < r \leq r_4, \\ 0 & \text{if } r_4 < r < \infty, \end{cases} \quad (10)$$

where $r_1, r_2, r_3, r_4, \bar{\zeta}_1, \bar{\zeta}_2, \bar{\zeta}_3$, and $\bar{\zeta}_4$ are specified constants. We assume that all basic state vortices have the same far-field circulation, specified by the choice $r_4\bar{v}_4 = r_{\text{ref}}\bar{v}_{\text{ref}}$, with $r_{\text{ref}} = 100$ km and $\bar{v}_{\text{ref}} = 20$ m s^{−1}. In this way, the mesoscale structure of the basic state vorticity field can be varied in a wide variety of ways, but the circulation $2\pi r\bar{v}(r)$ for $r \geq 100$ km is fixed at $2\pi r_{\text{ref}}\bar{v}_{\text{ref}} = 4\pi \times 10^6$ m² s^{−1}. In other words, all the basic state vortices considered here have the same “synoptic scale environment” but have different “mesoscale distributions” of vorticity inside $r = 100$ km.

By restricting this analysis to the class of perturbations whose disturbance vorticity arises solely through radial displacement of the basic state vorticity, the perturbation

vorticity vanishes everywhere except near the edges of the constant vorticity regions, i.e., (1) reduces to $\nabla^2 \psi' = 0$ for $r \neq r_1, r_2, r_3, r_4$, or equivalently, (2) reduces to

$$\frac{d}{dr} \left(r \frac{d\hat{\psi}^{(m)}}{dr} \right) - \frac{m^2}{r^2} \hat{\psi}^{(m)} = 0 \quad \text{for } r \neq r_1, r_2, r_3, r_4. \quad (11)$$

The general solution of (11) in the five regions separated by the radii r_1, r_2, r_3, r_4 can be constructed from different linear combinations of r^m and r^{-m} in each region. An alternative and physically more revealing approach is to write the general solution of (11), valid in any of the five regions, as a linear combination of the four (i.e., $j = 1, 2, 3, 4$) basis functions $B_j^{(m)}(r)$, defined by

$$B_j^{(m)}(r) = \begin{cases} (r/r_j)^m & 0 \leq r \leq r_j, \\ (r_j/r)^m & r_j \leq r < \infty. \end{cases} \quad (12)$$

The solutions for $\hat{\psi}^{(m)}(r)$ and $\psi'(r, \phi, t)$ are then

$$\hat{\psi}^{(m)}(r) = \sum_{j=1}^4 \Psi_j^{(m)} B_j^{(m)}(r) \quad \text{and} \quad \psi'(r, \phi, t) = \sum_{j=1}^4 \Psi_j^{(m)} B_j^{(m)}(r) e^{i(m\phi - \nu^{(m)}t)}, \quad (13)$$

where $\Psi_1^{(m)}, \Psi_2^{(m)}, \Psi_3^{(m)}, \Psi_4^{(m)}$ are complex coefficients. Since $dB_j^{(m)}/dr$ is discontinuous at $r = r_j$, the solution associated with the coefficient $\Psi_j^{(m)}$ has vorticity anomalies concentrated at $r = r_j$ and the corresponding streamfunction decays away in both directions from $r = r_j$. Plots of the basis functions $B_j^{(m)}(r)$ are shown in Figure 6 for both a wide moat case (upper panel) where $(r_1, r_2, r_3, r_4) = (10, 20, 50, 60)$ km and a narrow moat case (lower panel) where $(r_1, r_2, r_3, r_4) = (10, 20, 30, 40)$ km. In the wide moat case the basis functions $B_2^{(m)}(r)$ and $B_3^{(m)}(r)$ have small amplitude in the moat, particularly for large values of m . As we shall see, unstable coupling of the pair of Rossby waves centered at $r = r_2$ and $r = r_3$ tends to occur only when the moat is narrow, and then primarily for the low wavenumber case $m = 2$.

In order to relate the four complex coefficients $\Psi_1^{(m)}, \Psi_2^{(m)}, \Psi_3^{(m)}$, and $\Psi_4^{(m)}$, integrate (2) over the narrow radial intervals centered at r_j to obtain the jump conditions

$$\lim_{\epsilon \rightarrow 0} \left\{ (\nu^{(m)} - m\bar{\omega}_j) r_j \left[\frac{d\hat{\psi}^{(m)}}{dr} \right]_{r_j-\epsilon}^{r_j+\epsilon} \right\} + (\bar{\zeta}_{j+1} - \bar{\zeta}_j) m \hat{\psi}^{(m)}(r_j) = 0 \quad \text{for } j = 1, 2, 3, 4, \quad (14)$$

where $\bar{\omega}_j = \bar{\omega}(r_j) = \bar{v}_j/r_j$. Substitution of the solution (13) into the four jump conditions (14) yields the matrix eigenvalue problem

$$\begin{pmatrix} \frac{1}{2}(\bar{\zeta}_2 - \bar{\zeta}_1) + m\bar{\omega}_1 & \frac{1}{2}(\bar{\zeta}_2 - \bar{\zeta}_1)(r_1/r_2)^m & \frac{1}{2}(\bar{\zeta}_2 - \bar{\zeta}_1)(r_1/r_3)^m & \frac{1}{2}(\bar{\zeta}_2 - \bar{\zeta}_1)(r_1/r_4)^m \\ \frac{1}{2}(\bar{\zeta}_3 - \bar{\zeta}_2)(r_1/r_2)^m & \frac{1}{2}(\bar{\zeta}_3 - \bar{\zeta}_2) + m\bar{\omega}_2 & \frac{1}{2}(\bar{\zeta}_3 - \bar{\zeta}_2)(r_2/r_3)^m & \frac{1}{2}(\bar{\zeta}_3 - \bar{\zeta}_2)(r_2/r_4)^m \\ \frac{1}{2}(\bar{\zeta}_4 - \bar{\zeta}_3)(r_1/r_3)^m & \frac{1}{2}(\bar{\zeta}_4 - \bar{\zeta}_3)(r_2/r_3)^m & \frac{1}{2}(\bar{\zeta}_4 - \bar{\zeta}_3) + m\bar{\omega}_3 & \frac{1}{2}(\bar{\zeta}_4 - \bar{\zeta}_3)(r_3/r_4)^m \\ -\frac{1}{2}\bar{\zeta}_4(r_1/r_4)^m & -\frac{1}{2}\bar{\zeta}_4(r_2/r_4)^m & -\frac{1}{2}\bar{\zeta}_4(r_3/r_4)^m & -\frac{1}{2}\bar{\zeta}_4 + m\bar{\omega}_4 \end{pmatrix} \begin{pmatrix} \Psi_1^{(m)} \\ \Psi_2^{(m)} \\ \Psi_3^{(m)} \\ \Psi_4^{(m)} \end{pmatrix} = \nu^{(m)} \begin{pmatrix} \Psi_1^{(m)} \\ \Psi_2^{(m)} \\ \Psi_3^{(m)} \\ \Psi_4^{(m)} \end{pmatrix}. \quad (15)$$

With the basic state vortex given by (10), we can solve the eigenvalue problem (15) once we have specified the azimuthal wavenumber m and the eight basic state vortex parameters $r_1, r_2, r_3, r_4, \bar{\zeta}_1, \bar{\zeta}_2, \bar{\zeta}_3$, and $\bar{\zeta}_4$. The eigenvalue problem (15) could be put in a dimensionless form, which would reveal the dynamic similarity of barotropic instability on a wide range of horizontal scales and time scales. However, to interpret the instability results in terms of tropical cyclones, it is useful to present results in dimensional form by choosing the numerical values $r_{\text{ref}} = 100$ km and $\bar{v}_{\text{ref}} = 20$ m s⁻¹, reasonable values for a major hurricane with concentric eyewalls.

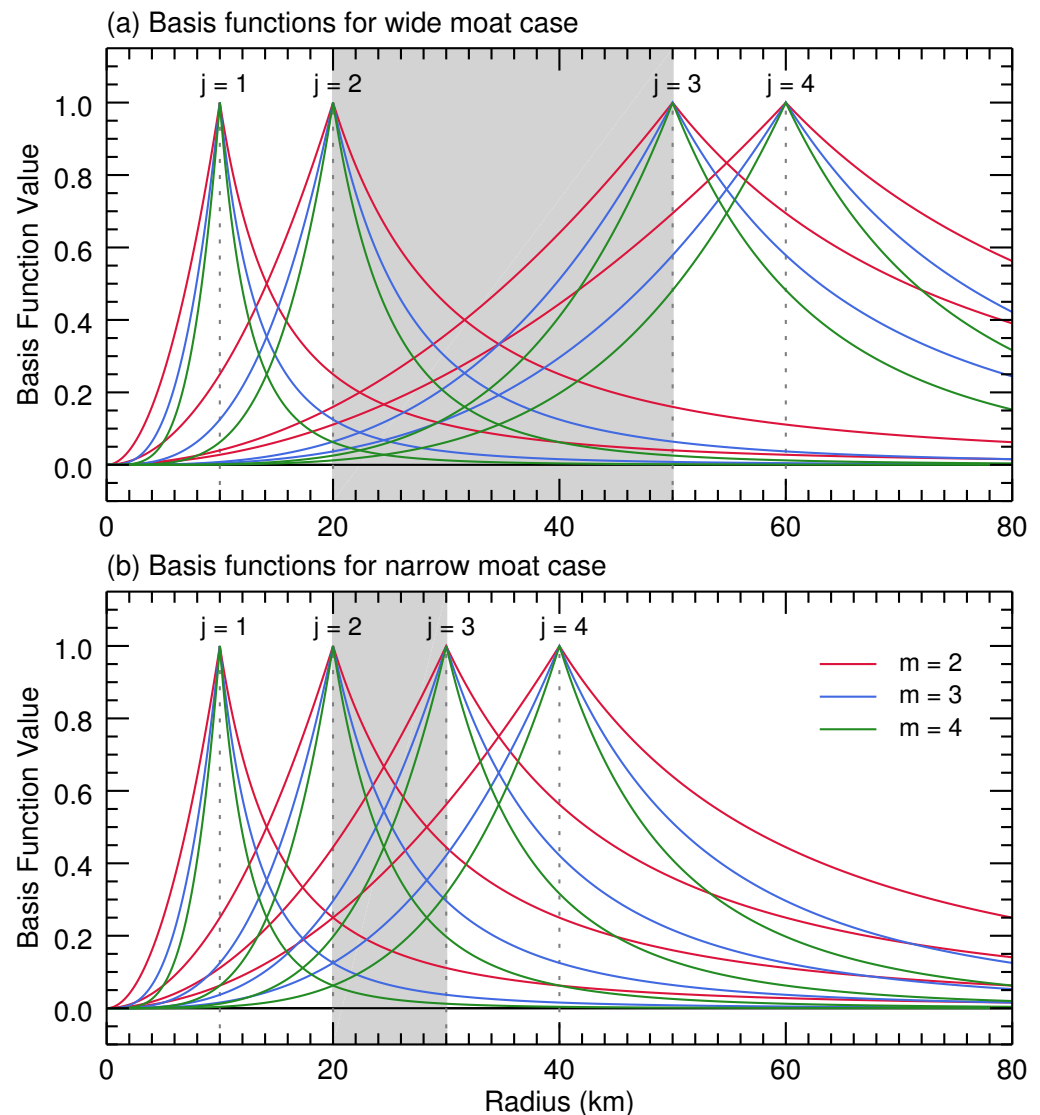


Figure 6. Basis functions $B_j^{(m)}(r)$ for (a) a wide moat case with $(r_1, r_2, r_3, r_4) = (10, 20, 50, 60)$ km, and for (b) a narrow moat case with $(r_1, r_2, r_3, r_4) = (10, 20, 30, 40)$ km. According to the first entry in (13), the radial structure function $\hat{\psi}^{(m)}(r)$ is a linear combination of these basis functions. These curves serve as measures of the potential coupling of Rossby waves on the interfaces $j = 1, 2, 3, 4$. For example, the potential coupling of $j = 1$ waves with $j = 4$ waves is weak, while the potential coupling of waves across the moat (shaded region) can be strong, particularly for $m = 2$ in the narrow moat case. However, it should be noted that the most unstable wavenumber is not always $m = 2$, since the eigenvalues and eigenvectors of the 4×4 matrix in (15) also depend on the basic state vorticity values $\bar{\zeta}_1, \bar{\zeta}_2, \bar{\zeta}_3$, and $\bar{\zeta}_4$.

The time dependence of $\psi'(r, \phi, t)$ is given by $e^{-iv^{(m)}t} = e^{-iv_r^{(m)}t} e^{iv_i^{(m)}t}$, where $v_r^{(m)}$ and $v_i^{(m)}$ are the real and imaginary parts of a generally complex eigenvalue $v^{(m)}$. Basic state flows that result in $v_i^{(m)} = 0$ for all four eigenvalues of every m are exponentially stable flows that allow propagating Rossby waves. A simple example of such a stable flow is the monopolar vortex with $\bar{\zeta}_2 - \bar{\zeta}_1 = \bar{\zeta}_3 - \bar{\zeta}_2 = \bar{\zeta}_4 - \bar{\zeta}_3 = -\bar{\zeta}_4 < 0$, in which case the matrix in (15) is symmetric no matter what values of r_1, r_2, r_3 , and r_4 are chosen, thereby guaranteeing that all four eigenvalues are real for every m .

The axisymmetric five-region vorticity distribution (10) contains the four variable geometrical parameters r_1, r_2, r_3 , and r_4 and the four variable vorticity parameters $\bar{\zeta}_1, \bar{\zeta}_2, \bar{\zeta}_3$, and $\bar{\zeta}_4$. For the present discussion, we have reduced this eight-parameter collection of

vortices down to a two-dimensional family of vortices by fixing some of the parameters to values informed by the data for Hurricane Maria. In particular, we have narrowed the number of variable geometrical parameters from four to one by choosing $r_1 = 7.5$ km, $r_2 = 12.5$ km, $17.5 \leq r_3 \leq 62.5$ km, and $r_4 = r_3 + 10$ km, so that the inner vorticity ring is 5 km wide, the outer ring is 10 km wide, and the moat width ($r_3 - r_2$) varies between 5 km and 50 km (the abscissa in Figures 7 and 8). We have also narrowed the number of variable vorticity parameters from four to one. This was performed by first noting that the integration of $d(r\bar{v}) = \bar{\zeta} r dr$ from $r = 0$ to $r = r_2$ and then from $r = r_2$ to $r = r_{\text{ref}}$ yields

$$\int_0^{r_2} \bar{\zeta} r dr = r_2 \bar{v}_2 \quad \text{and} \quad \int_{r_2}^{r_{\text{ref}}} \bar{\zeta} r dr = r_{\text{ref}} \bar{v}_{\text{ref}} - r_2 \bar{v}_2. \quad (16)$$

Assuming $\bar{\zeta}_1 = \alpha \bar{\zeta}_2$ and $\bar{\zeta}_3 = \gamma \bar{\zeta}_4$, it is physically reasonable to consider values of the constants α and γ in the range $0 \leq \alpha \leq 1$ and $0 \leq \gamma \leq 1$. For the calculations presented here, we have chosen $\alpha = 0.5$ and $\gamma = 0.2$. Evaluating the integrals in (16), we obtain

$$\bar{\zeta}_2 = \frac{2r_2 \bar{v}_2}{r_2^2 - (1 - \alpha)r_1^2} \quad \text{and} \quad \bar{\zeta}_4 = \frac{2(r_{\text{ref}} \bar{v}_{\text{ref}} - r_2 \bar{v}_2)}{\gamma(r_3^2 - r_2^2) + (r_4^2 - r_3^2)}. \quad (17)$$

Thus, once the constants $r_1, r_2, r_3, r_4, r_{\text{ref}}, \bar{v}_{\text{ref}}, \alpha$, and γ have been specified, the four vorticity parameters $\bar{\zeta}_1, \bar{\zeta}_2, \bar{\zeta}_3$, and $\bar{\zeta}_4$ are seen to depend on the parameter \bar{v}_2 , which we shall choose to be in the range $15 \leq \bar{v}_2 \leq 75 \text{ m s}^{-1}$ (the ordinate in Figures 7 and 8). The relations $r_2 \bar{v}_2 = r_1 \bar{v}_1 + \frac{1}{2} \bar{\zeta}_2 (r_2^2 - r_1^2)$ and $r_4 \bar{v}_4 = r_{\text{ref}} \bar{v}_{\text{ref}}$ can be written in the respective forms

$$\begin{aligned} \bar{v}_1 &= \left(\frac{\alpha r_1 r_2}{r_2^2 - (1 - \alpha)r_1^2} \right) \bar{v}_2 = \left(\frac{15}{41} \right) \bar{v}_2, \\ \bar{v}_4 &= \left(\frac{r_{\text{ref}}}{r_2 + (r_3 - r_2) + (r_4 - r_3)} \right) \bar{v}_{\text{ref}} = \frac{2000}{22.5 + (r_3 - r_2)}, \end{aligned} \quad (18)$$

where the final equalities make use of the assumptions $\alpha = 0.5$, $r_1 = 7.5$ km, $r_2 = 12.5$ km, $r_4 - r_3 = 10$ km, $r_{\text{ref}} = 100$ km, and $\bar{v}_{\text{ref}} = 20 \text{ m s}^{-1}$. Based on (18), we conclude that the inner eyewall basic state velocity maximum \bar{v}_2 can also be interpreted in terms of the basic state velocity \bar{v}_1 , as given in the right ordinate of Figure 7, while the moat width $r_3 - r_2$ can also be interpreted in terms of the outer eyewall wind maximum \bar{v}_4 , as given in the upper abscissa of Figure 7. Isolines of \bar{v}_3 are given by the curved blue lines in Figure 7, while the curved red line connects points for which $\bar{v}_2 = \bar{v}_4$, with the upper-right region corresponding to $\bar{v}_2 > \bar{v}_4$ (stronger inner-eyewall winds) and the lower-left region corresponding to $\bar{v}_2 < \bar{v}_4$ (stronger outer-eyewall winds). Figure 7 summarizes the five-region, basic state vortex structure for each member of the vortex family being considered. For a given point (vortex) on this diagram, we can find \bar{v}_1 from the scale on the right, \bar{v}_2 from the scale on the left, \bar{v}_3 from the curved blue lines, and \bar{v}_4 from the scale at the top. The associated radii are $r_1 = 7.5$ km, $r_2 = 12.5$ km, and $r_4 - r_3 = 10$ km, with the moat width taken from the scale at the bottom. Three specific basic state vortices (A, B, and C) are defined in Table 2 and correspond to the three points indicated in Figures 7 and 8.

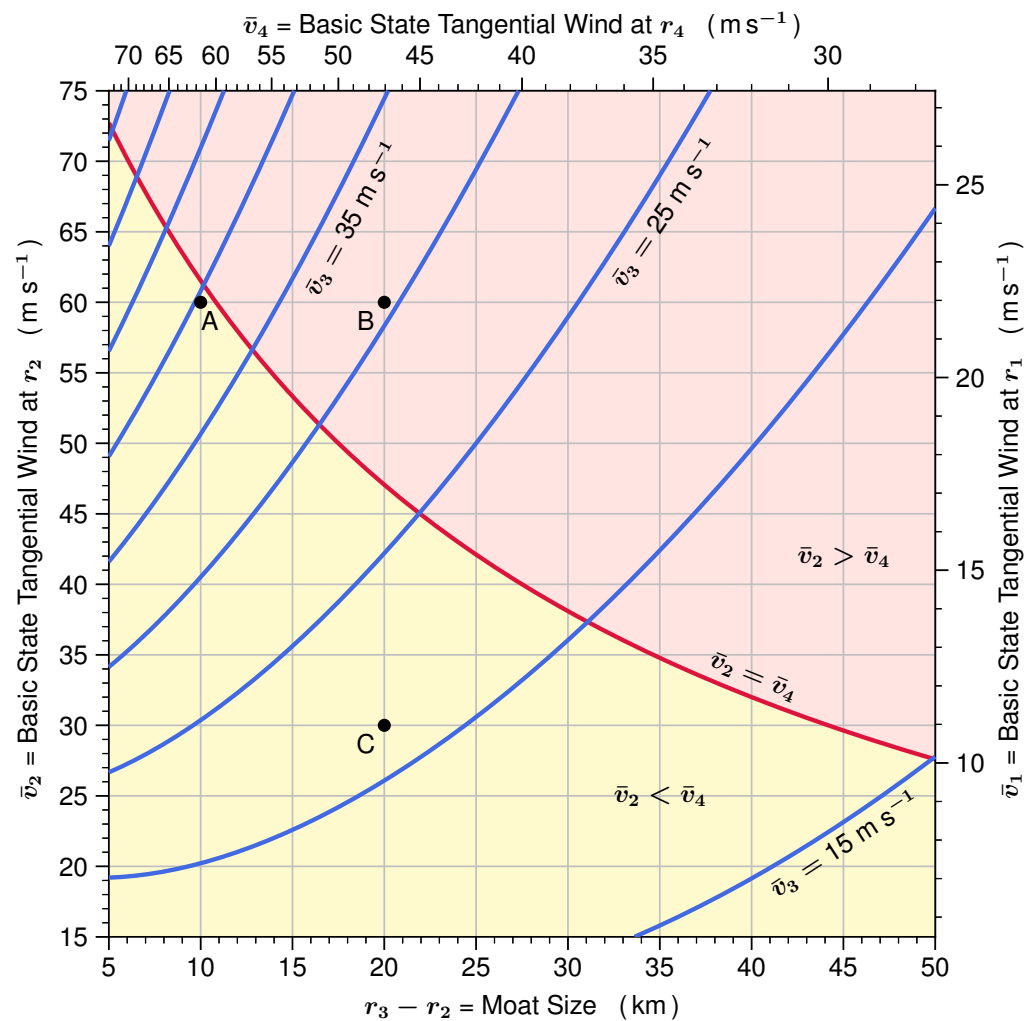


Figure 7. Basic state structure diagram for the family of basic state vortices with $\alpha = 0.5$, $\gamma = 0.2$, $r_{\text{ref}} = 100$ km, $\bar{v}_{\text{ref}} = 20$ m s^{−1}, $r_1 = 7.5$ km, $r_2 = 12.5$ km, $r_4 - r_3 = 10$ km, and for moat widths $r_3 - r_2$ ranging from 5 to 50 km (lower abscissa) and inner core tangential wind maxima ranging from 15 to 75 m s^{−1} (left ordinate). Using (18) the abscissa can also be interpreted as \bar{v}_4 (top axis) and the ordinate as \bar{v}_1 (right axis). Isolines of \bar{v}_3 are given by the curved blue lines, shown every 5 m s^{−1} from 15 m s^{−1} to 55 m s^{−1}. The curved red line connects points for which $\bar{v}_2 = \bar{v}_4$, with the upper-right region (shaded red) corresponding to $\bar{v}_2 > \bar{v}_4$ (stronger inner-eyewall winds) and the lower-left region (shaded yellow) corresponding to $\bar{v}_2 < \bar{v}_4$ (stronger outer-eyewall winds). The three points indicated in the diagram correspond to the three basic state vortices listed in Table 2.

It is important to note that, although the radar and flight data for Hurricane Maria, as shown in Figures 2–4, provide a useful guide for determining the parameters needed to model Maria as an axisymmetric five-region vortex, this data does not completely define these parameters. In particular, the data provides more guidance about the radial parameters than about the vorticity parameters. Vortex A is chosen to be a reasonable Maria-like vortex (when Maria was approximately axisymmetric early in the time period shown in Figure 2). Vortex B is then chosen to be similar to Vortex A but with a larger moat, and Vortex C to be similar to Vortex B but weaker.

Once the 4×4 matrix in (15) is defined, the solution of the eigenvalue problem yields four values of the complex frequency $\nu^{(m)}$, each with a corresponding eigenvector. We have solved this problem using both the Wolfram Mathematica software package and the NumPy package for the Python programming language. As a check on the eigenvalues, we have confirmed that the sum of the eigenvalues equals the trace of the matrix, i.e.,

$v_1^{(m)} + v_2^{(m)} + v_3^{(m)} + v_4^{(m)} = m(\bar{\omega}_1 + \bar{\omega}_2 + \bar{\omega}_3 + \bar{\omega}_4) - \frac{1}{2}\bar{\zeta}_1$. For a given m , there are three possible patterns for the eigenvalue set: (i) all four eigenvalues are real, which is the pattern obtained for an exponentially stable basic state; (ii) two eigenvalues are real and the other two are complex conjugates; (iii) all four eigenvalues are complex, with two pairs of complex conjugates. Most of the basic state vortex parameter space explored here yields either Pattern (i) (stable vortex flows, even though the Rayleigh necessary condition for instability is satisfied) or Pattern (ii) (one unstable mode). Pattern (iii) is less common, but can occur, for example, when the moat is very wide and there are essentially independent instabilities across both vorticity rings. A given basic state vortex may have multiple instabilities for different values of m . The maximum instability or most unstable mode for such a vortex is the value of m with the largest value of $v_i^{(m)}$.

Table 2. Summary of the parameters for three basic state vortex cases: Vortex A (narrow moat; intense vortex), Vortex B (wide moat; intense vortex), Vortex C (wide moat; weak vortex). The second through tenth columns, respectively give the basic state tangential velocity \bar{v}_2 for the inner ring; the radii r_1 , r_2 , r_3 , and r_4 of the interfaces between regions; the reference tangential velocity \bar{v}_{ref} and reference radius r_{ref} ; and the constants α and γ . Note that for each of these basic state vortices, r_1 , r_2 , \bar{v}_{ref} , r_{ref} , α , and γ are held constant and r_3 and r_4 are constrained such that the width of the outer ring $r_4 - r_3$ is also held constant.

Case	\bar{v}_2 (m s ^{−1})	r_1 (km)	r_2 (km)	r_3 (km)	r_4 (km)	\bar{v}_{ref} (m s ^{−1})	r_{ref} (km)	α	γ
Vortex A	60.0	7.5	12.5	22.5	32.5	20.0	100.0	0.5	0.2
Vortex B	60.0	7.5	12.5	32.5	42.5	20.0	100.0	0.5	0.2
Vortex C	30.0	7.5	12.5	32.5	42.5	20.0	100.0	0.5	0.2

Figure 8 provides a stability diagram for the family of basic state vortices shown in Figure 7, showing the azimuthal wavenumber m (via the shaded regions) and the growth rate $v_i^{(m)}$ (via the white contour lines) associated with the maximum instability of each vortex in this family. A simple and useful interpretation is that there are three distinct types of instability. The first type involves the interaction of Rossby waves at r_3 and r_4 , i.e., across the outer ring of elevated vorticity. In Figure 8, the maximum instability occurs as this first type for tangential wavenumbers $m = 4, 5, \dots, 12$ in the blue region, primarily on the bottom and right half of the stability diagram. The second type of instability occurs when the moat is narrow and involves the interaction of Rossby waves at r_2 and r_3 , i.e., across the moat. In Figure 8, the maximum instability occurs as this second type for tangential wavenumbers $m = 2, 3, 4, 5$ in the red region. The third type of instability involves the interaction of vorticity waves at r_1 and r_2 , i.e., across the inner ring of elevated vorticity. In Figure 8, the maximum instability occurs as this third type only for tangential wavenumber $m = 4$ in the yellow region. The next subsection examines the energetics of the linear dynamics and provides a useful tool for determining to which vortex region a particular instability applies.

For interpretation of the eyewall cycle in Hurricane Maria, the red region of Figure 8 is of most interest. This region corresponds to narrow moats and is dominated by wavenumber-two instability across the moat. As an example indicative of observations shown in Figure 4, consider Vortex A, labeled A in Figures 7 and 8, given by $\bar{v}_2 = 60 \text{ m s}^{-1}$ and $r_3 - r_2 = 10 \text{ km}$. This point lies near the middle of the red region and has $v_i^{(2)} = 2.79 \text{ h}^{-1}$, i.e., it corresponds to an $m = 2$ instability with an e -folding time of $1/v_i^{(2)} = 0.36 \text{ h}$. The real part of the corresponding eigenfunction $\psi'(r, \phi, t)$, given by (13), is shown in Figure 9. Since the largest values of ψ' occur in the moat region $r_2 \leq r \leq r_3$, this unstable mode can be considered as an interaction of vortex Rossby waves at $r = r_2$ and $r = r_3$. For this unstable mode the flow in the inner eyewall ($r_1 < r < r_2$) is strongly outward in the SW and NE quadrants and is strongly inward in the NW and SE quadrants. Barring too much

deformation due to differential rotation, the high vorticity in the inner ring will be distorted into a highly elliptical shape. This will be confirmed by the non-linear numerical model simulation presented in Section 3.

Finally, note that, although we only present linear stability results for one specific two-dimensional family of vortices here, we did investigate other families (based on different choices of the parameters r_1 , \dots , and γ that are not necessarily guided by reasonable values for Hurricane Maria) and found that the wavenumber-2 instability across the moat is a common feature for strong vortices with narrow moats in many such families.

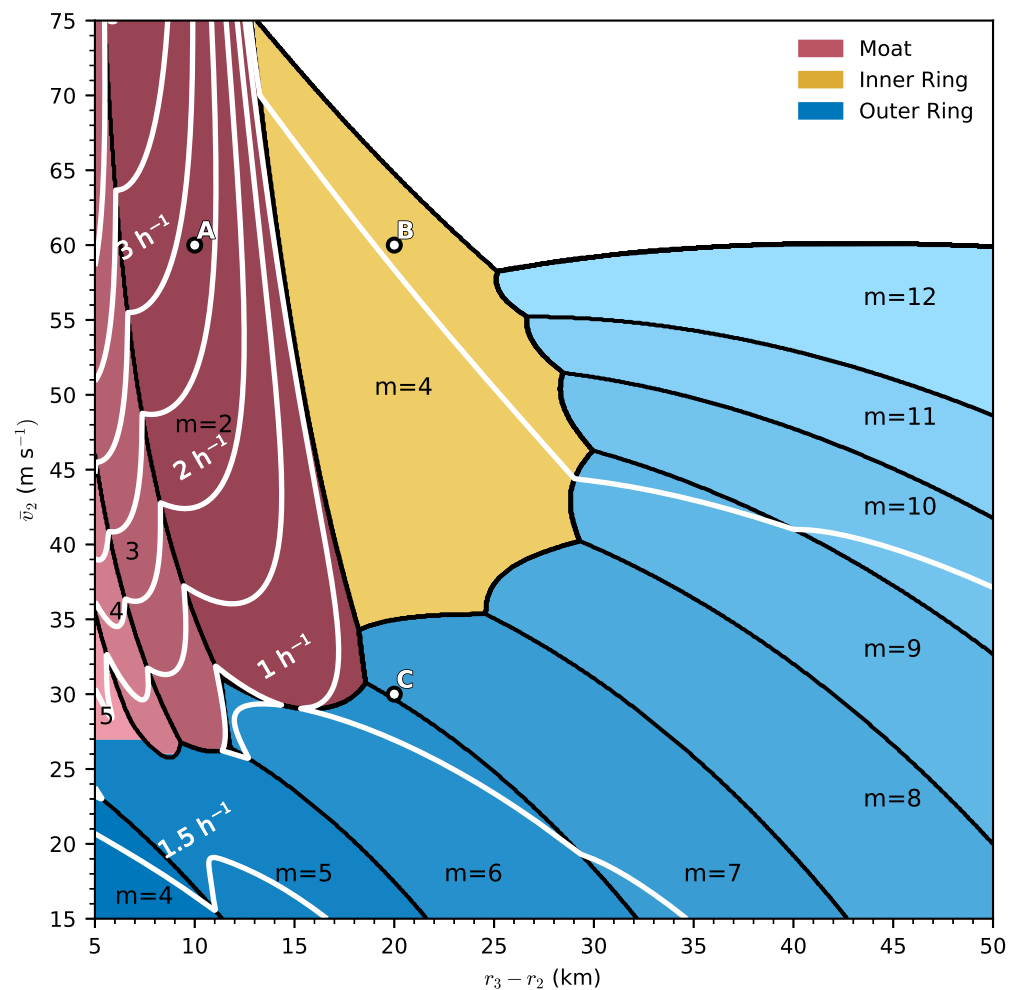


Figure 8. Stability diagram for the family of basic state vortices shown in Figure 7. The shaded regions indicate the azimuthal wavenumber (for $2 \leq m \leq 12$) of the maximum instability for each vortex in this family. The solid white curves are isolines of the growth rate for this maximum instability (i.e., the largest value of $v_i^{(m)}$ for each vortex in this family), shown from 0.5 h^{-1} to 4.0 h^{-1} with an interval of 0.5 h^{-1} . The region shaded red indicates that the maximum instability occurs across the moat. This region occurs when the moat is narrow, is dominated by azimuthal wavenumber $m = 2$ instability across the moat, and is the main region of interest in this study. The regions shaded blue and yellow indicate that the maximum instability occurs across the outer or inner ring, respectively. The three circles correspond to the basic state vortex cases (A, B, C) listed in Table 2.

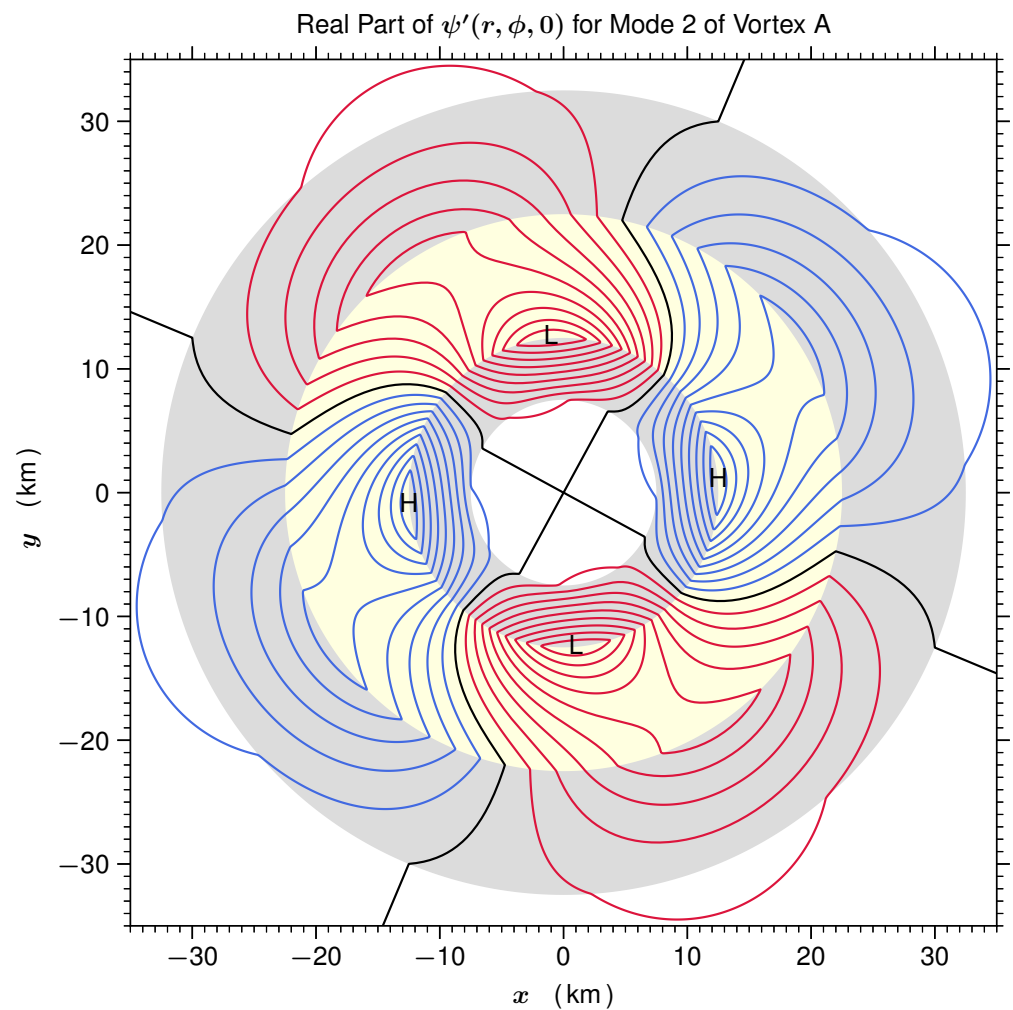


Figure 9. Real part of the initial eigenfunction $\psi'(r, \phi, 0)$ corresponding to the $m = 2$ instability across the moat for Vortex A, as defined by $(r_1, r_2, r_3, r_4) = (7.5, 12.5, 22.5, 32.5)$ km and $\bar{v}_2 = 60 \text{ m s}^{-1}$. The inner and outer rings of the five-region model are shaded in gray, and the moat region is shaded in yellow. The blue isolines are for $\psi' > 0$, the black isoline for $\psi' = 0$, and the red isolines for $\psi' < 0$. The perturbation velocity $(u', v') = (-\partial\psi'/r\partial\phi, \partial\psi'/\partial r)$ is clockwise around the high and anticlockwise around the low. The inner eyewall ($7.5 < r < 12.5$ km) has two regions of strong radial outflow and two regions of strong radial inflow, producing a rapid distortion of the inner eyewall into an elliptical shape. The e -folding time for this $m = 2$ eigenfunction is $1/v_i^{(2)} = 0.36$ h, and the local period of oscillation is $2\pi/v_r^{(2)} = 0.365$ h, so the whole structure rotates anticlockwise once in 0.73 h. In the moat region ($22.5 < r < 32.5$ km), the isolines of ψ' tilt against the basic state differential rotation, i.e., $(d\bar{\omega}/dr) < 0$ and $\overline{u'v'} > 0$, so this region is responsible for most (91.8%) of the conversion of basic state kinetic energy to eddy kinetic energy.

2.3. Energetics of the Linear Dynamics

To better understand the conversion of basic state kinetic energy to eddy kinetic energy, multiply (1) by $-\psi'$ to obtain

$$\frac{\partial}{\partial t} \left(\frac{1}{2} \nabla \psi' \cdot \nabla \psi' \right) = \nabla \cdot (\psi' \nabla \psi_t') + \frac{\partial}{\partial \phi} \left(\bar{\omega} \psi' \zeta' - \frac{d\bar{\zeta}}{r dr} \frac{1}{2} \psi'^2 \right) + \bar{\omega} r u' \zeta'. \quad (19)$$

Integrating (19) over the entire domain, noting that only the first and last terms survive, we obtain

$$\begin{aligned} \frac{d\mathcal{E}_e}{dt} = C \quad \text{where} \quad \mathcal{E}_e = \int_0^{2\pi} \int_0^\infty \frac{1}{2} \nabla \psi' \cdot \nabla \psi' r dr d\phi, \\ \text{and} \quad C = 2\pi \int_0^\infty \bar{\omega} r \overline{u' \zeta'} r dr, \quad \overline{u' \zeta'} = \frac{1}{2\pi} \int_0^{2\pi} u' \zeta' d\phi, \end{aligned} \quad (20)$$

with \mathcal{E}_e denoting the eddy kinetic energy and C the conversion rate between basic state and eddy kinetic energy. The radial flux of vorticity is related to the radial flux of angular momentum by

$$r u' \zeta' = \frac{\partial(r u' \mathcal{M}')}{r \partial r} + \frac{\partial[\frac{1}{2}(v'^2 - u'^2)]}{\partial \phi} \implies \overline{r u' \zeta'} = \frac{\partial(\overline{r u' \mathcal{M}'})}{r \partial r}, \quad (21)$$

where $\mathcal{M}' = r v'$ is the eddy angular momentum. Using (21) and an integration by parts, the energy conversion term can also be written as

$$C = 2\pi \int_0^\infty \left(-\frac{d\bar{\omega}}{dr} \right) \overline{u' \mathcal{M}'} r dr. \quad (22)$$

Note that $C > 0$ when there is a preponderance of regions in which $(d\bar{\omega}/dr) \overline{u' \mathcal{M}'} < 0$. Referring to Figure 5, $(d\bar{\omega}/dr) < 0$ in the moat, so that the moat contributes to $C > 0$ when $\overline{u' \mathcal{M}'} > 0$, i.e., an outward radial flux of angular momentum. This occurs when the troughs and ridges in ψ' tilt anticlockwise with increasing r , i.e., the troughs and ridges tilt against the differential rotation, as in the moat region of Figure 9.

The radial flux of angular momentum can be computed from the real part of ψ' , which is

$$\psi' = \left[\hat{\psi}_r^{(m)} \cos(m\phi - \nu_r^{(m)} t) - \hat{\psi}_i^{(m)} \sin(m\phi - \nu_r^{(m)} t) \right] e^{\nu_i^{(m)} t}. \quad (23)$$

Using (23) in $r u' = -(\partial \psi' / \partial \phi)$ and $v' = (\partial \psi' / \partial r)$, we obtain

$$r u' = m \left[\hat{\psi}_r^{(m)} \sin(m\phi - \nu_r^{(m)} t) + \hat{\psi}_i^{(m)} \cos(m\phi - \nu_r^{(m)} t) \right] e^{\nu_i^{(m)} t}, \quad (24)$$

$$\mathcal{M}' = r \left[\frac{d\hat{\psi}_r^{(m)}}{dr} \cos(m\phi - \nu_r^{(m)} t) - \frac{d\hat{\psi}_i^{(m)}}{dr} \sin(m\phi - \nu_r^{(m)} t) \right] e^{\nu_i^{(m)} t}. \quad (25)$$

Taking the product of (24) and (25) and then integrating over ϕ , we obtain

$$\overline{r u' \mathcal{M}'} = \frac{1}{2} m r e^{2\nu_i^{(m)} t} \left(\hat{\psi}_i^{(m)} \frac{d\hat{\psi}_r^{(m)}}{dr} - \hat{\psi}_r^{(m)} \frac{d\hat{\psi}_i^{(m)}}{dr} \right) = \frac{1}{2} m r e^{2\nu_i^{(m)} t} \text{Imag} \left\{ \hat{\psi}^{(m)} \frac{d\hat{\psi}^{(m)*}}{dr} \right\}. \quad (26)$$

In the five-region model, Equation (21) takes a simple form because $\zeta' = 0$ for $r \neq r_1, r_2, r_3$, and r_4 . Thus, $\overline{r u' \zeta'} = 0$ in each of the five regions, but $\overline{r u' \zeta'}$ is very large over the thin regions surrounding r_1, r_2, r_3 , and r_4 . Thus, from (21), $\overline{r u' \mathcal{M}'}$ is piecewise constant, with discontinuities at r_1, r_2, r_3 , and r_4 , which allows (22) to be written as $C = C_1 + C_2 + C_3 + C_4 + C_5$, where

$$C_j = 2\pi (\bar{\omega}_{j-1} - \bar{\omega}_j) \left(\overline{r u' \mathcal{M}'} \right)_j \quad \text{for } j = 1, 2, 3, 4, 5, \quad (27)$$

with $\left(\overline{r u' \mathcal{M}'} \right)_j$ denoting the constant value of $\overline{r u' \mathcal{M}'}$ in region j , and $\bar{\omega}_j$ denoting the basic state angular velocity at the point $r = r_j$. Both $\left(\overline{r u' \mathcal{M}'} \right)_1$ and $\left(\overline{r u' \mathcal{M}'} \right)_5$ vanish, so that the innermost and outermost regions do not contribute to C . To determine which of the other

three regions is most responsible for growth of the eddy kinetic energy, we have used (26) and the solution (13) to compute $ru'\mathcal{M}'$, with the result that

$$\left(\overline{ru'\mathcal{M}'}\right)_j = m^2 e^{2v_i^{(m)}t} \begin{cases} P_{1,2}^{(m)} + P_{1,3}^{(m)} + P_{1,4}^{(m)} & \text{if } j = 2, \\ P_{1,3}^{(m)} + P_{2,3}^{(m)} + P_{1,4}^{(m)} + P_{2,4}^{(m)} & \text{if } j = 3, \\ P_{1,4}^{(m)} + P_{2,4}^{(m)} + P_{3,4}^{(m)} & \text{if } j = 4, \end{cases} \quad (28)$$

where $P_{j,k}^{(m)} = (r_j/r_k)^m \text{Imag}\{\Psi_j^{(m)}\Psi_k^{(m)*}\}$. For the example shown in Figure 9, namely $m = 2$ for Vortex A, we obtain

$$(C_1, C_2, C_3, C_4, C_5) = (0.000, 0.0779, 0.9182, 0.0039, 0.000) C,$$

as shown in Table 3. The dominance of C_3 is consistent with calling this example a “wavenumber-two instability across the moat.” A further appreciation of the fact that the moat is the seat of this particular instability is obtained by noting that the moat ($r_2 \leq r \leq r_3$) is only 35.0% of the area of the energetically active region ($r_1 \leq r \leq r_4$), but it accounts for 91.8% of the kinetic energy conversion. Table 3 summarizes the linear stability results for the specific Vortices A, B, and C, as defined in Table 2. In particular, note that Vortex A (a strong vortex with a narrow moat) has a strong $m = 2$ instability across the moat, but Vortex B (a similarly strong vortex but with a wider moat) does not have an instability across the moat.

Table 3. Summary of the linear eigenvalue analysis for Vortex A (narrow moat; intense vortex), Vortex B (wide moat; intense vortex), and Vortex C (wide moat; weak vortex). For each instability, the second through seventh columns, respectively, give the azimuthal wavenumber m , the exponential growth rate $v_i^{(m)}$, the e -folding time $1/v_i^{(m)}$ in hours, the percentage of the energy conversion from the inner eyewall (C_2/C), from the moat (C_3/C), and from the outer eyewall (C_4/C). Vortex A, with a moat only 10 km wide, is unstable to both azimuthal wavenumbers $m = 2$ and $m = 4$, with the $m = 4$ structure having an e -folding time of 1.07 h and most of its energy conversion in the inner eyewall, while the $m = 2$ structure has a faster e -folding time of 0.36 h and most of its energy conversion in the moat. In contrast, Vortex B, with its wider 20 km moat, does not produce $m = 2$ instability across the moat but does produce $m = 4$ instability across the inner ring. The weaker Vortex C produces four different instabilities, including $m = 2$ instability primarily across the moat, but this $m = 2$ instability is the weakest of the four instabilities that also include $m = 4$ across the inner ring and $m = 6$ and $m = 7$ across the outer ring.

Vortex	m	$v_i^{(m)}$ (h ^{−1})	$2/v_i^{(m)}$ (h)	C_2/C (%)	C_3/C (%)	C_4/C (%)
A	2	2.79	0.36	7.79	91.82	0.39
	4	0.94	1.07	99.67	0.33	0.00
B	4	0.44	2.28	100.00	0.00	0.00
C	2	0.61	1.65	6.69	84.54	8.77
	4	0.73	1.36	99.98	0.02	0.00
	6	0.84	1.20	0.00	0.00	100.00
	7	0.86	1.17	0.00	0.00	100.00

3. Non-Linear Simulation of Barotropic Instability across the Moat

To isolate the barotropic aspects of the non-linear evolution, we now consider the non-divergent barotropic model with ordinary diffusion. Expressing the velocity components

in terms of the streamfunction by $u = -(\partial\psi/\partial y)$ and $v = (\partial\psi/\partial x)$, we can write the non-divergent barotropic model as

$$\frac{\partial\zeta}{\partial t} + \frac{\partial(\psi, \zeta)}{\partial(x, y)} = \nu \nabla^2 \zeta, \quad \text{where} \quad \nabla^2 \psi = \zeta. \quad (29)$$

Note that throughout this paper the symbols u, v are used to denote eastward and northward components of velocity when using Cartesian coordinates and to denote radial and tangential components when using polar coordinates. In addition, the symbol ν in this section is used to denote the constant diffusion coefficient (rather than an eigenvalue). We shall now present numerical integrations of (29) that demonstrate the process by which an unstable concentric eyewall structure leads to a vorticity rearrangement that forms a more dynamically stable structure. To obtain solutions, we employ a finite-difference model on a domain of size 600×600 km with 2048×2048 equally spaced grid cells with a constant streamfunction for the boundary condition. The model uses the fourth-order Arakawa Jacobian [71,72], nine-point stencil Laplacian [73], and multigrid methods from MUDPACK version five [74] to solve the elliptic equation $\nabla^2 \psi = \zeta$. The model uses a standard fourth-order Runge–Kutta scheme for time differencing. For the results from the finite-difference model, the simulations use a time step of 1.875 s and viscosity in (29) of $\nu = 2.75 \text{ m}^2 \text{ s}^{-1}$. This value of ν suppresses noise for waves less than $2\Delta x, 2\Delta y$ —similar to a pseudo-spectral model resolving 1024×1024 Fourier modes—and prevents enstrophy from accumulating at small scales. For a comparison of the finite-difference and pseudo-spectral non-divergent barotropic models, see supplementary file S1.

As the initial condition for (29), we use a smoothed version of (10), with the initial axisymmetric vorticity field given by

$$\bar{\zeta}(x, y, 0) = \begin{cases} \bar{\zeta}_1 & \text{if } 0 \leq r \leq r_1 - d, \\ \bar{\zeta}_1 S((r - r_1 + d)/2d) + \bar{\zeta}_2 S((r_1 + d - r)/2d) & \text{if } r_1 - d \leq r \leq r_1 + d, \\ \bar{\zeta}_2 & \text{if } r_1 + d \leq r \leq r_2 - d, \\ \bar{\zeta}_2 S((r - r_2 + d)/2d) + \bar{\zeta}_3 S((r_2 + d - r)/2d) & \text{if } r_2 - d \leq r \leq r_2 + d, \\ \bar{\zeta}_3 & \text{if } r_2 + d \leq r \leq r_3 - d, \\ \bar{\zeta}_3 S((r - r_3 + d)/2d) + \bar{\zeta}_4 S((r_3 + d - r)/2d) & \text{if } r_3 - d \leq r \leq r_3 + d, \\ \bar{\zeta}_4 & \text{if } r_3 + d \leq r \leq r_4 - d, \\ \bar{\zeta}_4 S((r - r_4 + d)/2d) & \text{if } r_4 - d \leq r \leq r_4 + d, \\ 0 & \text{if } r_4 + d \leq r, \end{cases} \quad (30)$$

where $S(s) = 1 - 3s^2 + 2s^3$ is the basic cubic Hermite shape function satisfying $S(0) = 1$, $S(1) = 0$, $S'(0) = S'(1) = 0$. This axisymmetric five-region vorticity distribution involves the specified constants $d, r_1, r_2, r_3, r_4, \bar{\zeta}_1, \bar{\zeta}_2, \bar{\zeta}_3$, and $\bar{\zeta}_4$. The new smoothing parameter is chosen to be $d = 1$ km, which results in a 2 km smoothing interval between each of the five regions. The other geometrical parameters are chosen to be the same as those used in Section 2 and listed in Table 2. We then enforce the constraints in (16), where again the reference radius r_{ref} is taken as 100 km and the reference tangential wind \bar{v}_{ref} is taken as 20 m s^{-1} . The inner eyewall wind maximum parameter is chosen to be $\bar{v}_2 = 60 \text{ m s}^{-1}$ for Vortices A and B and $\bar{v}_2 = 30 \text{ m s}^{-1}$ for Vortex C. Substituting (30) into the constraints (16), we obtain

$$\begin{aligned} \mathcal{A}\bar{\zeta}_2 + \mathcal{B}\bar{\zeta}_4 &= r_2 \bar{v}_2, \\ \mathcal{C}\bar{\zeta}_2 + \mathcal{D}\bar{\zeta}_4 &= r_{\text{ref}} \bar{v}_{\text{ref}} - r_2 \bar{v}_2, \end{aligned} \quad (31)$$

where the constants $\mathcal{A}, \mathcal{B}, \mathcal{C}$, and \mathcal{D} are defined in Appendix A. In summary, after specification of $r_{\text{ref}} \bar{v}_{\text{ref}}$, and r_2 and \bar{v}_2 , the right-hand sides in (31) are fixed and the values of $\bar{\zeta}_2$ and $\bar{\zeta}_4$ are easily computed from (31), after which $\bar{\zeta}_1$ and $\bar{\zeta}_3$ are computed from $\bar{\zeta}_1 = 0.5 \bar{\zeta}_2$ and $\bar{\zeta}_3 = 0.2$ and $\bar{\zeta}_4$.

For the first experiment, the numerical integration is performed using the smoothed version of Vortex A as the initial condition, so that $\{r_1, r_2, r_3, r_4\} = \{7.5, 12.5, 22.5, 32.5\}$ km, $d = 1.0$ km, and $\{\tilde{\zeta}_1, \tilde{\zeta}_2, \tilde{\zeta}_3, \tilde{\zeta}_4, \tilde{\zeta}_5\} = \{60.62, 121.24, 7.60, 37.98, 0.0\} \times 10^{-4} \text{ s}^{-1}$. The resulting initial condition is shown by the red curve in Figure 10. This tangential wind profile is generally similar to the observed profiles from the WC-130J radial flight into Hurricane Maria on 20 September 2017 (as shown in Figure 3). Figure 11 shows results of this experiment in the form of vorticity maps plotted for $t = 0, 10$ –18, and 48 h. The growth of the wavenumber-two maximum instability becomes evident as the inner eyewall distorts into an elongated elliptical shape. An animation of these vorticity maps for Vortex A with a 15 min. time resolution is available as described in the Data Availability Statement.

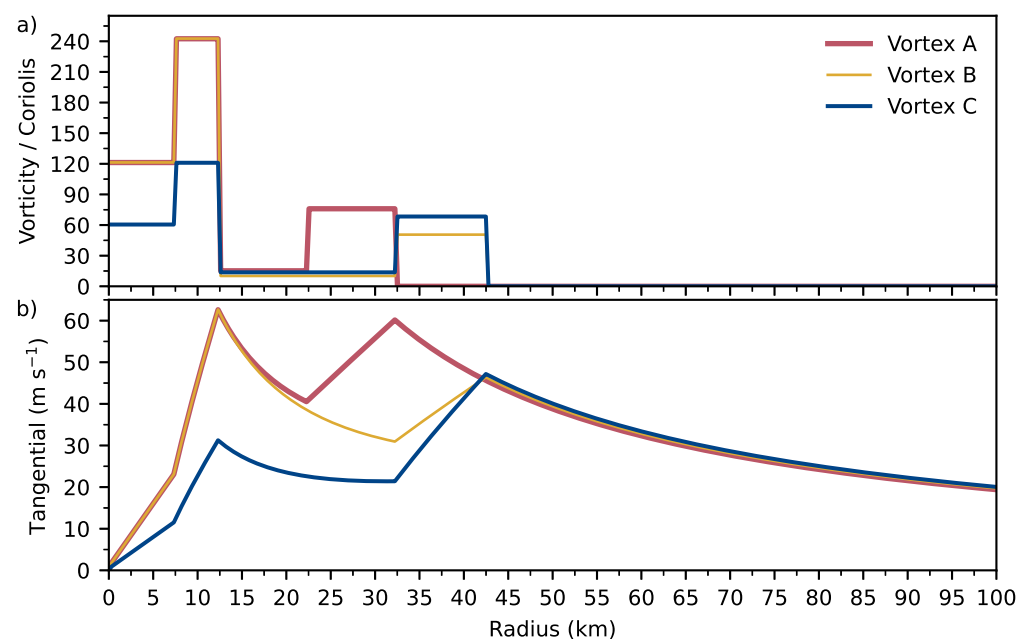


Figure 10. Initial (a) vorticity and (b) tangential wind profiles for the smoothed versions of the three basic state vortex cases given in Table 2 where $\bar{v}_2 = 60 \text{ m s}^{-1}$ and $r_3 - r_2 = 10 \text{ km}$ for Vortex A (red curve), $\bar{v}_2 = 60 \text{ m s}^{-1}$ and $r_3 - r_2 = 20 \text{ km}$ for Vortex B (yellow curve), $\bar{v}_2 = 30 \text{ m s}^{-1}$ and $r_3 - r_2 = 20 \text{ km}$ for Vortex C (blue curve), and the constant parameters shared by the family of vortices are $\alpha = 0.5$, $\gamma = 0.2$, $r_{\text{ref}} = 100 \text{ km}$, $\bar{v}_{\text{ref}} = 20 \text{ m s}^{-1}$, $r_1 = 7.5 \text{ km}$, $r_2 = 12.5 \text{ km}$, $r_4 = r_3 + 10 \text{ km}$, and $d = 1 \text{ km}$.

Since no asymmetric perturbations have been added to the axisymmetric initial condition (30), the exponential instability must grow from very small model truncation errors. As a result of not introducing an azimuthally broad-banded perturbation to a circular vorticity distribution, the truncation errors resulting from grid discretization and domain shape assist in exciting the multiple modes, notably wavenumbers $m = 2, 4$ in the moat and inner and outer rings, respectively. However, with the growth rates from the linear stability analysis being small or zero for $m = 4$, the wavenumber $m = 2$ instability, once excited, dominates the simulation and initiates potential vorticity mixing. Approximately 10 h of model integration are required before the $m = 2$ instability begins to be apparent. The instability then develops rapidly, and by $t = 11 \text{ h}$ the inner eyewall has been stretched and is now bordered by two pools of low vorticity from the original moat. At $t = 12 \text{ h}$, two regions of low vorticity from the vortex environment are being entrained, and at $t = 13 \text{ h}$ there are four regions of low vorticity (pale green) as the vortex core consolidates. Between 14 h and 18 h, a filamented tripole structure emerges. Although the limitations of existing observational techniques make it difficult to directly observe tripole structures, the ubiquitous nature of these structures in numerical model simulations and laboratory experiments indicate that they are probably common in tropical cyclones.

As an introduction to the extensive literature on tripoles, see [70,75–83]. Between 24 h and 48 h, the basic tripole structure persists, but becomes less filamented as both the interior vortex and Gibbs phenomena in the environment are smoothed by the diffusion term.

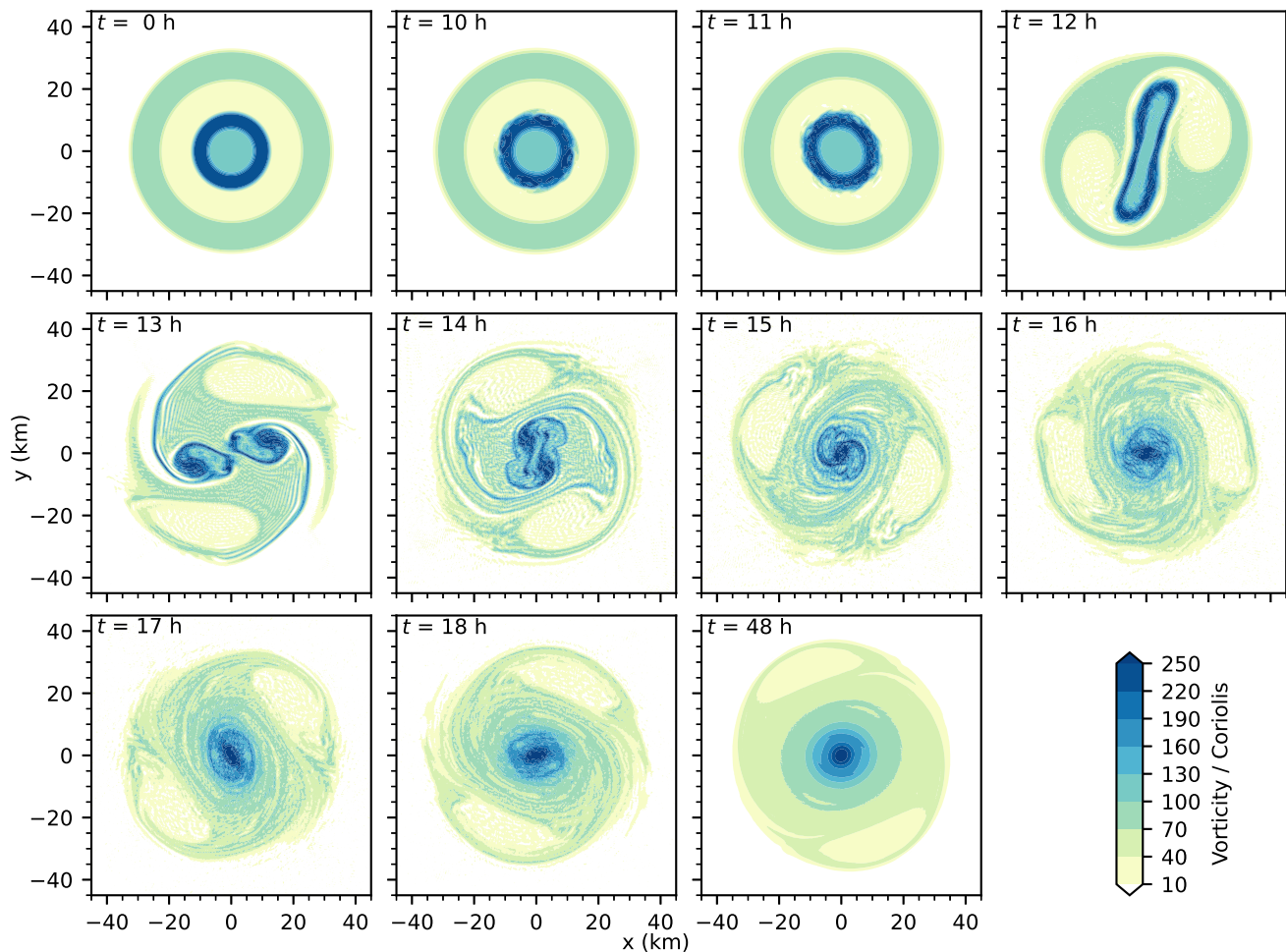


Figure 11. Evolution of the vorticity field in the finite-difference non-divergent barotropic model initialized with the smoothed version (30) of Vortex A, using the parameters $(r_1, r_2, r_3, r_4) = (7.5, 12.5, 22.5, 32.5)$ km and $d = 1$ km. The panels are for $t = 0, 10$ – 18 , and 48 h from the top left to the bottom right to show the initial condition, mixing process, and end of the simulation.

Further insight into the non-linear evolution, illustrated in Figure 11, can be obtained using concepts from two-dimensional geophysical turbulence theory. The analysis begins by noting that two integral properties associated with (29) are the kinetic energy and enstrophy relations

$$\frac{d\mathcal{E}}{dt} = -2\nu\mathcal{Z} \quad \text{and} \quad \frac{d\mathcal{Z}}{dt} = -2\nu\mathcal{P}, \quad (32)$$

where

$$\mathcal{E} = \iint \frac{1}{2}(\nabla\psi \cdot \nabla\psi) dx dy, \quad \mathcal{Z} = \iint \frac{1}{2}\zeta^2 dx dy, \quad \mathcal{P} = \iint \frac{1}{2}(\nabla\zeta \cdot \nabla\zeta) dx dy \quad (33)$$

are the kinetic energy, the enstrophy, and the palinstrophy. Because the right-hand sides of the two equations in (32) are always negative, the kinetic energy \mathcal{E} and enstrophy \mathcal{Z} both decay with time. However, the integrations shown here exhibit “selective decay,” i.e., the

enstrophy decays much faster than the kinetic energy. One way to understand this is to note that the evolution of the palinstrophy \mathcal{P} is governed by

$$\frac{d\mathcal{P}}{dt} = - \iint \left[u_x \zeta_x^2 + (v_x + u_y) \zeta_x \zeta_y + v_y \zeta_y^2 \right] dx dy - \nu \iint \left(\nabla^2 \zeta \right)^2 dx dy. \quad (34)$$

Although the last term in (34) always acts as a damping effect, \mathcal{P} can rapidly increase due to the first term on the right-hand side. For small enough values of ν , the palinstrophy can surge to values much larger than its initial value. When \mathcal{P} is large, the enstrophy \mathcal{Z} decays rapidly in comparison with \mathcal{E} , whose rate of decay becomes smaller as \mathcal{Z} becomes smaller.

Figure 12 shows the time evolution of the area-integrated kinetic energy $\mathcal{E}(t)$, enstrophy $\mathcal{Z}(t)$, and palinstrophy $\mathcal{P}(t)$ as well as the domain maximum wind for the numerical experiments involving the smoothed versions of Vortices A, B, and C, given in Table 2, as initial conditions. The barotropic instability process leads to an active cascade of the spectral distribution of enstrophy to high wavenumbers, where dissipation operates to decrease the area-integrated enstrophy. For Vortex A, the decrease in area-integrated enstrophy is $\sim 30\%$. This is in marked contrast to the area-integrated kinetic energy, which tends to be a rugged integral, decreasing by only $\sim 0.3\%$. The rapid decrease in the area-integrated enstrophy $\mathcal{E}(t)$ begins near $t = 12$ h, when the palinstrophy $\mathcal{P}(t)$ pulses to large values due to the highly filamented nature of the flow.

For Vortices B and C, instability is weaker and the filamentation process does not result in the same high-palinstrophy episodes seen in Vortex A. However, the instability does eventually develop across the regions expected from the linear stability analysis, as summarized in Table 3, and can be interpreted in the context of previous work [52,53]. In Vortex B, the wavenumber $m = 4$ pattern develops across the inner ring causing mixing to reorganize the inner-core vorticity into a monopole-like structure while leaving the outer ring intact. In Vortex C, a wavenumber $m = 8$ pattern develops in the outer ring that causes the vorticity from the outer ring to contract. After this period of mixing, the inner ring develops a wavenumber $m = 2$ pattern. There are two potential interpretations for the development of this $m = 2$ pattern in Vortex C: (1) the growth rate for $m = 2$, given in Table 3, is slow and takes until near the end of the simulation to develop; (2) the smaller moat created by the contraction of the outer-ring vorticity shifts Vortex C to the left in Figures 7 and 8, causing the $m = 2$ instability to become more unstable. For animations of Vortices B and C, see the Data Availability Statement.

Idealized integrations such as these raise the question of whether real tropical cyclones experience high-palinstrophy episodes when the potential vorticity field is rapidly rearranged due to dynamic instability. If tropical cyclones really experience high- and low-palinstrophy periods and associated intensity variations, new observational methods would probably be required to capture such structures so that they could be introduced into analysis and initialization methods for numerical weather prediction.

Returning to Vortex A, the vortex becomes perched on the edge of dynamic instability as the inner-core wind maximum decreases and the moat narrows. After the linear phase of this exponential instability and the high-palinstrophy episode, the vortex evolves into a Rankine-like structure through homogenization of vorticity inside the outer eyewall. In effect, the instability across the outer ring and the instability across the moat are both removed in a single mixing process. During the mixing process, the domain wind maximum of the vortex briefly spikes before continuing to weaken (Figure 12d). This wind maximum evolution is different from Vortex B and C, which evolve in a manner more consistent with previous numerical simulations [52,53,84]. However, despite the spike, the kinetic energy remains invariant to localized wind fluctuations [85,86].

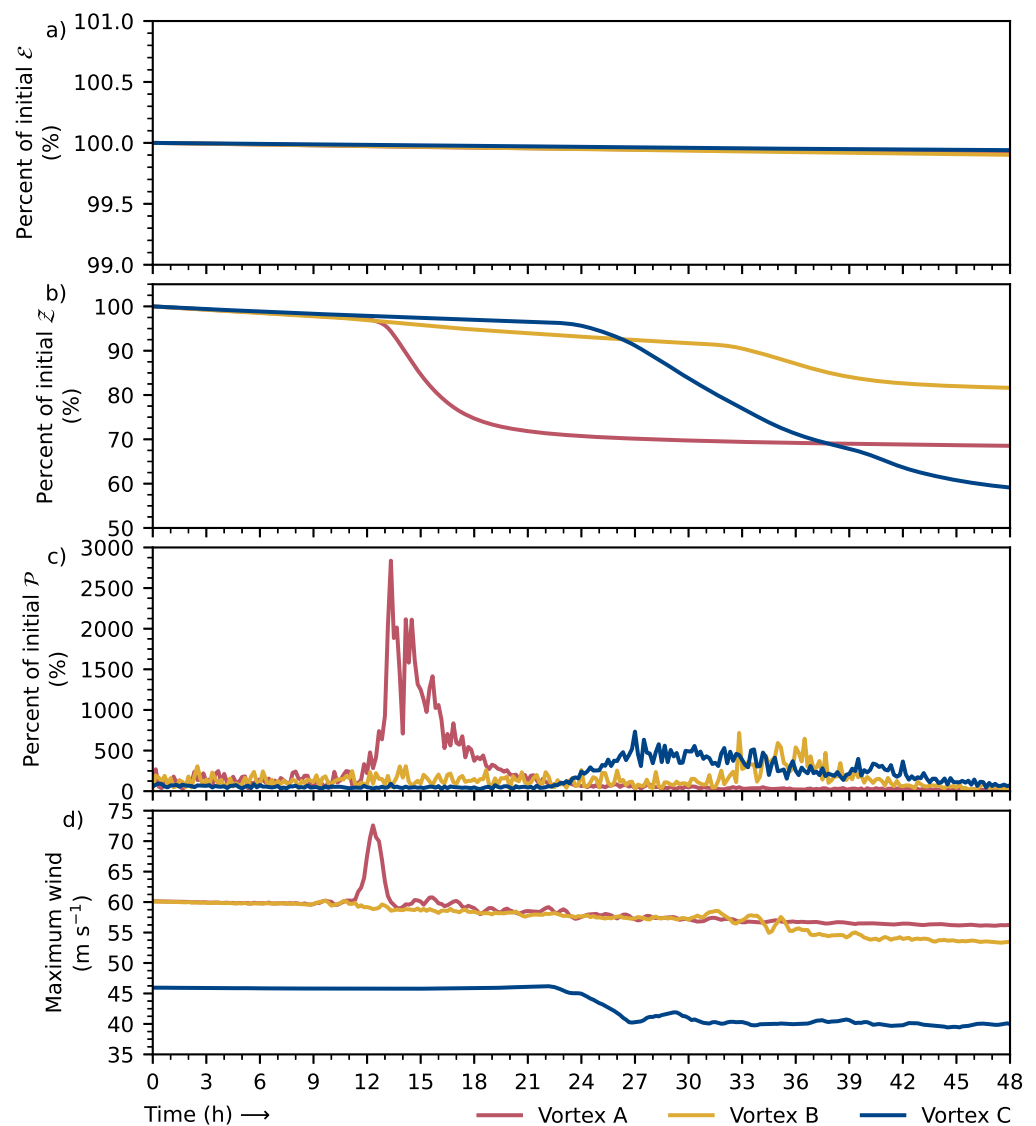


Figure 12. Time evolution of the area-integrated (a) kinetic energy $\mathcal{E}(t)$, (b) enstrophy $\mathcal{Z}(t)$, and (c) palinstrophy $\mathcal{P}(t)$, as defined in (33) as well as (d) the domain maximum wind for the smoothed versions of the three basic state vortex cases given in Table 2. Note the different scales, indicating that enstrophy selectively decays compared to energy. Also, the three curves in panel (c) are normalized by the initial palinstrophy for Vortex A.

The evolution of the ζ field in Figure 11 might be crudely described as a vorticity rearrangement in which the fluid with the largest vorticity ($\zeta = 240 f$ for $7.5 < r < 12.5$ km) exchanges position (with area conservation) with the fluid of the next largest vorticity ($\zeta = 120 f$ for $0 \leq r < 7.5$ km), and the low-vorticity fluid in the moat ($\zeta = 15 f$ for $12.5 < r < 22.5$ km) exchanges position with the fluid in the outer eyewall ($\zeta = 75 f$ for $22.5 < r < 32.5$ km). After this rearrangement, the final monopole has the five-region vorticity structure $\zeta/f = (240, 120, 75, 15, 0)$ with the four interfaces located at $r = (10.0, 12.5, 26.6, 32.5)$ km. Under this idealized rearrangement, the values of the enstrophy \mathcal{Z} at the initial and final states are equal, but the values of the kinetic energy \mathcal{E} at the initial and final states are not, even though the azimuthal wind is unchanged for $r = 12.5$ km and for $r \geq 32.5$ km. Thus, this simple rearrangement argument is flawed, being inconsistent with the selective decay concepts of two-dimensional turbulence. Improved models for the final state can be formulated from arguments based on the minimization of enstrophy with constrained circulation, energy, and/or angular momentum. Another,

more rigorous approach to predicting the final state is to maximize the Boltzmann mixing entropy subject to similar constraints on energy and angular momentum (for further details see Schubert et al. [52]). In passing, we note that barotropic instability across the moat, and the resulting vorticity rearrangement near the core of the tropical cyclone, probably do not have a major impact on the track of the cyclone, since the track depends more on the synoptic-scale steering flow rather than the turbulent motions in the storm's mesoscale power plant.

These results raise the possibility that barotropic instability and subsequent potential vorticity mixing is an important part of many concentric eyewall cycles. A better understanding of the universality of the concept of "wavenumber-two barotropic instability across the moat" might be obtained from the study of satellite microwave data taken near the end of concentric eyewall cycles, with the goal of identifying clearly elliptical patterns in the inner eyewall.

The asymmetries observed in the radar reflectivity patterns of Hurricane Maria (Figure 2) occurred as the storm passed south-west of St. Croix, an island $11 \text{ km} \times 35 \text{ km}$ with a maximum elevation of 355 m. The barotropic model results shown here indicate that vigorous dynamic instability can occur in tropical cyclones with narrow moats. Since the model used here does not include topographic effects, it can be argued that such "island effects" are not central to the dynamical processes observed in Figure 2. However, topographic effects could play a role in triggering the instability. It would be interesting to explore this possibility using more general dynamical models than the non-divergent model used here.

4. Concluding Remarks

As a concentric eyewall cycle is near completion, the previously well-defined inner eyewall often seems to fade away. Two interesting questions concern whether this demise of the inner eyewall occurs via an axisymmetric process or an asymmetric process, and what happens to the hollow tower of potential vorticity that was presumably associated with the inner eyewall. One possible answer is that the demise of the inner eyewall can sometimes occur asymmetrically, with the potential vorticity being filamented and mixed across the new eye. This scenario may in fact be common, and may have been observed in Hurricane Maria only because it occurred within range of a radar that could resolve it in space and time.

Using a family of idealized vortices with parameters motivated by the aircraft data collected in Hurricane Maria, the present study explored these questions within the simple framework of the non-divergent barotropic model, thereby attempting to better understand the fundamental interaction that can occur across the moat that separates concentric eyewalls. A linearized version of the barotropic model was used to simulate a hollow central vortex surrounded by a region of low vorticity, or moat, which in turn is surrounded by an annular ring of enhanced vorticity. This provides a basic state which can support three simple instability types. In the first type, phase locking occurs between vortex Rossby waves propagating along the inner and outer edges of the outer eyewall. In the second instability type, there is vortex Rossby wave interaction across the moat between the two eyewalls. In the third instability type, there is an analogous phase locking between waves on the inner and outer edges of the inner eyewall. Instability across the moat is most likely realized in azimuthal wavenumber-two, and non-linear model integrations show that subsequent mixing can disintegrate the inner vorticity ring. In this view, concentric eyewall structures are rich with possible dynamical instabilities, such that concentric eyewall cycles may sometimes end in an episode of hydrodynamic instability. While gleaned from a simple framework with a family of idealized vortices, this mechanism offers an explanation for the remarkable radar and aircraft data obtained in Hurricane Maria just before landfall in Puerto Rico. Note that there are other possible mechanisms that arise in more complicated models, e.g., the mechanism of spontaneous radiative imbalance [12,29,87,88]. This mechanism involves the interaction of a vortex Rossby wave

and an inertia-gravity wave, resulting in the spontaneous emission of the inertia-gravity wave and growth of the vortex Rossby wave. This type of dynamic cannot be studied with the non-divergent barotropic model, so the relative importance of spontaneous radiative imbalance and classical barotropic instability for Hurricane Maria remains an open question. Furthermore, additional work can be conducted with a Hurricane Maria-like family of vortices by stepping through a hierarchy of models as performed in analyzing full-physical model simulations [65].

It is interesting to note that the concentric eyewall cycle of Hurricane Maria (2017) was similar in certain respects to that of Hurricane Beulah (1967), a storm that passed south of Puerto Rico fifty years earlier. Although the Beulah case occurred before the era of modern Doppler weather radar, and although the center of Beulah did not pass closer than approximately 185 km to the San Juan radar, Hoose and Colón [89] were able to use the 34 h of radar reflectivity observations to document an entire concentric eyewall cycle. From their Figs. 6–9 and their associated discussion of aircraft reconnaissance data, a reasonable set of parameters for the stability analysis shown here in Figure 8 are $\bar{v}_2 \approx 50 \text{ m s}^{-1}$ and $(r_1, r_2, r_3, r_4) \approx (4, 11, 22, 39) \text{ km}$, such that the moat width is $r_3 - r_2 = 11 \text{ km}$. Assuming the other parameters used in the construction of Figure 8 are reasonable values for Beulah, this would place the storm's general structure in the region of Figure 8 corresponding to $m = 2$ barotropic instability across the moat. Although we lack high-resolution radar data from a large number of cases, it seems possible that this type of $m = 2$ instability across the moat is an important part of many concentric eyewall cycles.

The Hurricane Maria radar data discussed in Section 1 provides the motivation for this theoretical work and constitutes a serendipitous observation of barotropic instability across a narrow moat between concentric eyewalls. Similar events probably go undetected when they occur well out over the open ocean, which limits generalizations of this work. However, synthetic aperture radar (SAR) surface wind speed retrievals from tropical cyclone overpasses by low-Earth orbiters might provide the needed insight into concentric eyewalls [90]. These overpasses open up the possibility of at least obtaining snapshots of potential vorticity rearrangement events that leave a signature in the surface wind speed. Figure 13, also discussed in [91], shows a possible example—that of Typhoon Haishen at 21:17 UTC 5 September 2020—when the storm had a double eyewall structure with a narrow moat in the north-east quadrant, a wider moat in the south-west quadrant, and an elliptical distortion of the inner-eyewall structure. In Section 2, the Rayleigh and Fjørtoft necessary conditions for instability were discussed assuming the instability has a normal mode form, i.e., a form like Figure 9, in which the whole pattern uniformly rotates while growing exponentially over time. To discuss the instability properties of asymmetric flows, such as those for Typhoon Haishen shown in Figure 13, it would be useful in future work to apply the more general non-linear concepts of “Arnol’d conditions” [92–94] in conjunction with numerical simulations using a hierarchy of models.

If instability across the moat in a real hurricane were to actually result in a stable, long-lived tripole structure, it is interesting to speculate whether such a tripolar potential vorticity structure could be detected using our present technology of satellite, radar, dropsonde, and aircraft observations. The most successful study to date involving the construction of potential vorticity maps for an intense tropical cyclone is that of Martinez et al. [95], who were able to combine National Aeronautics and Space Administration WB-57 dropsonde data with NOAA WP-3D Doppler radar and in situ data to analyze the axisymmetric potential vorticity structure of Hurricane Patricia (2015) at several stages in its life cycle. Their study indicates that present technology is on the verge of resolving interesting potential vorticity structures, possibly including tripoles. However, even if we are unable to directly observe tripolar potential vorticity structures through detailed analysis of the wind field, the imprint of such potential vorticity structures might be detected in other fields such as the vertical motion and cloud fields. The relevant dynamics might be studied through solutions of an ω -equation, generalized so as to be applied to the high Rossby number curved flow in a tropical cyclone. The vertical variation of the vorticity advection

due to the tripole would provide a force for the ω -field, which would be augmented by diabatic processes and detectable in the convection field. An interesting challenge would be to separate such an effect from the important effect of large-scale environmental vertical shear on the vertical motion and cloud fields.

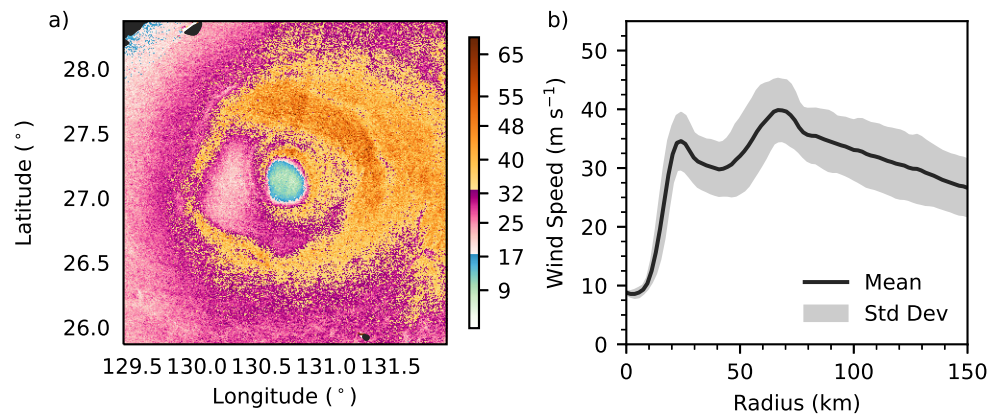


Figure 13. The left panel, (a), shows a SAR-derived (data from RADARSAT-2) surface wind speed map of Typhoon Haishen at 21:17 UTC 5 September 2020, when the storm had a double eyewall structure with a narrow moat in the north-east quadrant and a wider moat in the south-west quadrant. The right panel, (b), shows the azimuthal mean (black curve) and \pm one standard deviation (gray shading) radial profile of wind speed, indicating the double eyewall structure with peaks in wind speed at radii of 28 and 67 km, and a moat width of approximately 20 km based on the azimuthal mean. The well-defined moat in the south-west quadrant is roughly twice as wide as the moat in the north-east quadrant, indicating a possible preference for subsequent barotropic instability in the north-east quadrant. More information about this overpass is available from [91].

Supplementary Materials: The following supporting information can be downloaded at: <https://www.mdpi.com/article/10.3390/meteorology2020013/s1>, A Comparison of Numerics for the Non-divergent Barotropic Model. Reference [96] is cited in supplementary material.

Author Contributions: Based on their previous research, J.P.K. first recognized that the radar data for Hurricane Maria could be interpreted in terms of barotropic instability across the moat between concentric eyewalls. C.J.S. then performed detailed analyses of satellite, radar, and aircraft data for Maria. To confirm the results presented here, the linear stability analyses and the non-linear model integrations were performed with independent codes written by C.J.S. (using Python for the eigenvalue problem and Fortran for numerical integrations of a finite-difference/Arakawa Jacobian model) and by R.K.T. (using Mathematica for the eigenvalue problem). W.H.S. contributed to the theoretical aspects of this research. All authors have read and agreed to the published version of the manuscript.

Funding: This research was funded by the National Science Foundation under grant number AGS-1841326.

Data Availability Statement: The NOAA GOES-16 Advanced Baseline Imager L1b radiance products are available from the NOAA Comprehensive Large Array-data Stewardship System (CLASS) at <https://www.class.noaa.gov>. NOAA Next Generation Radar (NEXRAD) Level 2 Base Product data for the WSR-88D in San Juan, Puerto Rico (TJUA) is available from the NOAA National Centers for Environmental Information at <https://doi.org/10.7289/V5W9574V>. Air Force WC-130J aircraft data is available from the NOAA Hurricane Research Division at https://www.aoml.noaa.gov/hrd/Storm_pages/maria2017/. Synthetic aperture radar retrieved tropical cyclone wind data is available from the NOAA Center for Satellite Applications and Research at https://www.star.nesdis.noaa.gov/socd/mech/sar/AKDEMO_products/APL_winds/tropical/. Linear stability analysis output, non-divergent barotropic model output, and radar animations are available on Dryad at <https://doi.org/10.5061/dryad.fj6q573zw>.

Acknowledgments: The authors would like to thank Brian McNoldy and Stu Ostro for their insights on the Hurricane Maria radar data, shared with the scientific community through the Tropical-Storms Email List. We thank John Knaff and Alex Libardoni for their helpful comments on an early version of this manuscript and two anonymous reviews.

Conflicts of Interest: The authors declare no conflicts of interest. The funders had no role in the design of the study; in the collection, analyses, or interpretation of data; in the writing of the manuscript; or in the decision to publish the results. The scientific results and conclusions, as well as any views or opinions expressed herein, are those of the author(s) and do not necessarily reflect those of NOAA or the Department of Commerce.

Appendix A. Model Initial Condition

In order to make the axisymmetric part of the numerical model initial condition (30) a slightly smoothed version of the linear model basic state (10), we enforce the constraints (16), but with $\bar{\zeta}(r)$ given by (30) instead of (10). Making use of $\bar{\zeta}_1 = \alpha\bar{\zeta}_2$ and $\bar{\zeta}_3 = \gamma\bar{\zeta}_4$, this results in (31), with the four constant coefficients given by

$$\begin{aligned} \mathcal{A} &= \frac{1}{2}\alpha(r_1 - d)^2 + \int_{r_1-d}^{r_1+d} \left[\alpha S\left(\frac{r - r_1 + d}{2d}\right) + S\left(\frac{r_1 + d - r}{2d}\right) \right] r dr \\ &\quad + \frac{1}{2}[(r_2 - d)^2 - (r_1 + d)^2] + \int_{r_2-d}^{r_2} S\left(\frac{r - r_2 + d}{2d}\right) r dr, \\ \mathcal{B} &= \int_{r_2-d}^{r_2} \gamma S\left(\frac{r_2 + d - r}{2d}\right) r dr, \\ \mathcal{C} &= \int_{r_2}^{r_2+d} S\left(\frac{r - r_2 + d}{2d}\right) r dr, \\ \mathcal{D} &= \int_{r_2}^{r_2+d} \gamma S\left(\frac{r_2 + d - r}{2d}\right) r dr + \int_{r_3-d}^{r_3+d} \left[\gamma S\left(\frac{r - r_3 + d}{2d}\right) + S\left(\frac{r_3 + d - r}{2d}\right) \right] r dr \\ &\quad + \frac{1}{2}\gamma[(r_3 - d)^2 - (r_2 + d)^2] + \frac{1}{2}[(r_4 - d)^2 - (r_3 + d)^2] \\ &\quad + \int_{r_4-d}^{r_4+d} S\left(\frac{r - r_4 + d}{2d}\right) r dr. \end{aligned} \quad (\text{A1})$$

To summarize, the $\bar{\zeta}(r)$ field for the numerical model is constructed by first specifying $r_1, r_2, r_3, r_4, d, \alpha, \gamma, r_{\text{ref}}, \bar{v}_{\text{ref}}$, and \bar{v}_2 , then numerically computing $\mathcal{A}, \mathcal{B}, \mathcal{C}$, and \mathcal{D} from (A1), and finally computing $\bar{\zeta}_2$ and $\bar{\zeta}_4$ from (31). This procedure provides all the information needed for evaluation of (30). To see how the linear basic state vortex (10) is a special case, set $d = 0$, in which case (A1) reduces to

$$\mathcal{A} = \frac{1}{2}\alpha r_1^2 + \frac{1}{2}(r_2^2 - r_1^2), \quad \mathcal{B} = 0, \quad \mathcal{C} = 0, \quad \mathcal{D} = \frac{1}{2}\gamma(r_3^2 - r_2^2) + \frac{1}{2}(r_4^2 - r_3^2), \quad (\text{A2})$$

so that (31) reduces to (17).

References

1. Willoughby, H.E.; Clos, J.A.; Shoreibah, M.G. Concentric eye walls, secondary wind maxima, and the evolution of the hurricane vortex. *J. Atmos. Sci.* **1982**, *39*, 395–411. [\[CrossRef\]](#)
2. Black, M.L.; Willoughby, H.E. The concentric eyewall cycle of Hurricane Gilbert. *Mon. Weather Rev.* **1992**, *120*, 947–957. [\[CrossRef\]](#)
3. Samsury, C.E.; Zipser, E.J. Secondary wind maxima in hurricanes: Airflow and relationship to rainbands. *Mon. Weather Rev.* **1995**, *123*, 3502–3517. [\[CrossRef\]](#)
4. Dodge, P.; Burpee, R.W.; Marks, F.D., Jr. The kinematic structure of a hurricane with sea level pressure less than 900 mb. *Mon. Weather Rev.* **1999**, *127*, 987–1004. [\[CrossRef\]](#)
5. Rozoff, C.M.; Schubert, W.H.; Kossin, J.P. Some dynamical aspects of tropical cyclone concentric eyewalls. *Q. J. R. Meteorol. Soc.* **2008**, *134*, 583–593. [\[CrossRef\]](#)

6. Molinari, J.; Zhang, J.A.; Rogers, R.F.; Vollaro, D. Repeated eyewall replacement cycles in Hurricane Frances (2004). *Mon. Weather Rev.* **2019**, *147*, 2009–2022. [\[CrossRef\]](#)
7. Houze, R.A., Jr.; Chen, S.S.; Smull, B.F.; Lee, W.C.; Bell, M.M. Hurricane intensity and eyewall replacement. *Science* **2007**, *315*, 1235–1239. [\[CrossRef\]](#)
8. Hence, D.A.; Houze, R.A., Jr. Kinematic structure of convective-scale elements in the rainbands of Hurricanes Katrina and Rita (2005). *J. Geophys. Res.* **2008**, *113*, D15108. [\[CrossRef\]](#)
9. Judt, F.; Chen, S.S. Convectively generated potential vorticity in rainbands and formation of the secondary eyewall in Hurricane Rita of 2005. *J. Atmos. Sci.* **2010**, *67*, 3581–3599. [\[CrossRef\]](#)
10. Didlake, A.C., Jr.; Houze, R.A., Jr. Kinematics of the secondary eyewall observed in Hurricane Rita (2005). *J. Atmos. Sci.* **2011**, *68*, 1620–1636. [\[CrossRef\]](#)
11. Bell, M.M.; Montgomery, M.T.; Lee, W.C. An axisymmetric view of concentric eyewall evolution in Hurricane Rita (2005). *J. Atmos. Sci.* **2012**, *69*, 2414–2432. [\[CrossRef\]](#)
12. Menelaou, K.; Yau, M.K.; Martinez, Y. On the dynamics of the secondary eyewall genesis in Hurricane Wilma (2005). *Geophys. Res. Lett.* **2012**, *39*, L04801. [\[CrossRef\]](#)
13. Didlake, A.C., Jr.; Heymsfield, G.M.; Reasor, P.D.; Guimond, S.R. Concentric eyewall asymmetries in Hurricane Gonzalo (2014) observed by airborne radar. *Mon. Weather Rev.* **2017**, *145*, 729–749. [\[CrossRef\]](#)
14. Cha, T.Y.; Bell, M.M. Comparison of single-Doppler and multiple-Doppler wind retrievals in Hurricane Matthew (2016). *Atmos. Meas. Tech.* **2021**, *14*, 3523–3539. [\[CrossRef\]](#)
15. Shapiro, L.J.; Willoughby, H.E. The response of balanced hurricanes to local sources of heat and momentum. *J. Atmos. Sci.* **1982**, *39*, 378–394. [\[CrossRef\]](#)
16. Nong, S.; Emanuel, K. A numerical study of the genesis of concentric eyewalls in hurricanes. *Q. J. R. Meteorol. Soc.* **2003**, *129*, 3323–3338. [\[CrossRef\]](#)
17. Rozoff, C.M.; Schubert, W.H.; McNoldy, B.D.; Kossin, J.P. Rapid filamentation zones in intense tropical cyclones. *J. Atmos. Sci.* **2006**, *63*, 325–340. [\[CrossRef\]](#)
18. Rozoff, C.M.; Nolan, D.S.; Kossin, J.P.; Zhang, F.; Fang, J. The roles of an expanding wind field and inertial stability in tropical cyclone secondary eyewall formation. *J. Atmos. Sci.* **2012**, *69*, 2621–2643. [\[CrossRef\]](#)
19. Terwey, W.D.; Montgomery, M.T. Secondary eyewall formation in two idealized, full-physics modeled hurricanes. *J. Geophys. Res.* **2008**, *113*, D12112. [\[CrossRef\]](#)
20. Kuo, H.C.; Schubert, W.H.; Tsai, C.L.; Kuo, Y.F. Vortex interactions and barotropic aspects of concentric eyewall formation. *Mon. Weather Rev.* **2008**, *136*, 5183–5198. [\[CrossRef\]](#)
21. Kuo, H.C.; Chang, C.P.; Yang, Y.T.; Jiang, H.J. Western North Pacific typhoons with concentric eyewalls. *Mon. Weather Rev.* **2009**, *137*, 3758–3770. [\[CrossRef\]](#)
22. Kuo, H.C.; Tsujino, S.; Hsu, T.Y.; Peng, M.S.; Su, S.H. Scaling law for boundary layer inner eyewall pumping in concentric eyewalls. *J. Geophys. Res. Atmos.* **2022**, *127*, e2021JD035518. [\[CrossRef\]](#)
23. Moon, Y.; Nolan, D.S.; Iskandarani, M. On the use of two-dimensional incompressible flow to study secondary eyewall formation in tropical cyclones. *J. Atmos. Sci.* **2010**, *67*, 3765–3773. [\[CrossRef\]](#)
24. Martinez, Y.; Brunet, G.; Yau, M.K. On the dynamics of two-dimensional hurricane-like concentric rings vortex formation. *J. Atmos. Sci.* **2010**, *67*, 3253–3268. [\[CrossRef\]](#)
25. Martinez, Y.; Brunet, G.; Yau, M.K.; Wang, X. On the dynamics of concentric eyewall genesis: Space-time empirical normal modes diagnosis. *J. Atmos. Sci.* **2011**, *68*, 457–476. [\[CrossRef\]](#)
26. Abarca, S.F.; Corbosiero, K.L. Secondary eyewall formation in WRF simulations of Hurricanes Rita and Katrina (2005). *Geophys. Res. Lett.* **2011**, *38*, L07802. [\[CrossRef\]](#)
27. Wu, C.C.; Huang, Y.H.; Lien, G.Y. Concentric eyewall formation in Typhoon Sinlaku (2008). Part I: Assimilation of T-PARC data based on the ensemble Kalman filter (EnKF). *Mon. Weather Rev.* **2012**, *140*, 506–527. [\[CrossRef\]](#)
28. Huang, Y.H.; Montgomery, M.T.; Wu, C.C. Concentric eyewall formation in Typhoon Sinlaku (2008). Part II: Axisymmetric dynamical processes. *J. Atmos. Sci.* **2012**, *69*, 662–674. [\[CrossRef\]](#)
29. Menelaou, K.; Yau, M.K.; Martinez, Y. Impact of asymmetric dynamical processes on the structure and intensity change of two-dimensional hurricane-like annular vortices. *J. Atmos. Sci.* **2013**, *70*, 559–582. [\[CrossRef\]](#)
30. Sun, Y.Q.; Jiang, Y.; Tan, B.; Zhang, F. The governing dynamics of the secondary eyewall formation of Typhoon Sinlaku (2008). *J. Atmos. Sci.* **2013**, *70*, 3818–3837. [\[CrossRef\]](#)
31. Wang, H.; Wu, C.C.; Wang, Y. Secondary eyewall formation in an idealized tropical cyclone simulation: Balanced and unbalanced dynamics. *J. Atmos. Sci.* **2016**, *73*, 3911–3930. [\[CrossRef\]](#)
32. Wang, H.; Wang, Y.; Xu, J.; Duan, Y. The axisymmetric and asymmetric aspects of the secondary eyewall formation in a numerically simulated tropical cyclone under idealized conditions on an f -plane. *J. Atmos. Sci.* **2019**, *76*, 357–378. [\[CrossRef\]](#)
33. Tyner, B.; Zhu, P.; Zhang, J.A.; Gopalakrishnan, S.; Marks, F., Jr.; Tallapragada, V. A top-down pathway to secondary eyewall formation in simulated tropical cyclones. *J. Geophys. Res. Atmos.* **2018**, *123*, 174–197. [\[CrossRef\]](#)

34. Lai, T.K.; Menelaou, K.; Yau, M.K. Barotropic instability across the moat and inner eyewall dissipation: A numerical study of Hurricane Wilma (2005). *J. Atmos. Sci.* **2019**, *76*, 989–1013. [\[CrossRef\]](#)
35. Nolan, D.S.; Zhang, J.A.; Stern, D.P. Evaluation of planetary boundary layer parameterizations in tropical cyclones by comparison of in situ observations and high-resolution simulations of Hurricane Isabel (2003). Part I: Initialization, maximum winds, and the outer-core boundary layer. *Mon. Weather Rev.* **2009**, *137*, 3651–3674. [\[CrossRef\]](#)
36. Nolan, D.S.; Stern, D.P.; Zhang, J.A. Evaluation of planetary boundary layer parameterizations in tropical cyclones by comparison of in situ observations and high-resolution simulations of Hurricane Isabel (2003). Part II: Inner-core boundary layer and eyewall structure. *Mon. Weather Rev.* **2009**, *137*, 3675–3698. [\[CrossRef\]](#)
37. Smith, R.K.; Montgomery, M.T. Hurricane boundary-layer theory. *Q. J. R. Meteorol. Soc.* **2010**, *136*, 1665–1670. [\[CrossRef\]](#)
38. Abarca, S.F.; Montgomery, M.T. Essential dynamics of secondary eyewall formation. *J. Atmos. Sci.* **2013**, *70*, 3216–3230. [\[CrossRef\]](#)
39. Abarca, S.F.; Montgomery, M.T. Departures from axisymmetric balance dynamics during secondary eyewall formation. *J. Atmos. Sci.* **2014**, *71*, 3723–3738. [\[CrossRef\]](#)
40. Abarca, S.F.; Montgomery, M.T. Are eyewall replacement cycles governed largely by axisymmetric balance dynamics? *J. Atmos. Sci.* **2015**, *72*, 82–87. [\[CrossRef\]](#)
41. Kepert, J.D. How does the boundary layer contribute to eyewall replacement cycles in axisymmetric tropical cyclones? *J. Atmos. Sci.* **2013**, *70*, 2808–2830. [\[CrossRef\]](#)
42. Williams, G.J.; Taft, R.K.; McNoldy, B.D.; Schubert, W.H. Shock-like structures in the tropical cyclone boundary layer. *J. Adv. Model. Earth Syst.* **2013**, *5*, 338–353. [\[CrossRef\]](#)
43. Slocum, C.J.; Williams, G.J.; Taft, R.K.; Schubert, W.H. Tropical cyclone boundary layer shocks. *arXiv* **2014**, arXiv:1405.7939. <https://doi.org/10.48550/arXiv.1405.7939>.
44. Kossin, J.P.; Sitkowski, M. An objective model for identifying secondary eyewall formation in hurricanes. *Mon. Weather Rev.* **2009**, *137*, 876–892. [\[CrossRef\]](#)
45. Kossin, J.P.; Sitkowski, M. Predicting hurricane intensity and structure changes associated with eyewall replacement cycles. *Weather Forecast.* **2012**, *27*, 484–488. [\[CrossRef\]](#)
46. Sitkowski, M.; Kossin, J.P.; Rozoff, C.M. Intensity and structure changes during hurricane eyewall replacement cycles. *Mon. Weather Rev.* **2011**, *139*, 3829–3847. [\[CrossRef\]](#)
47. Sitkowski, M.; Kossin, J.P.; Rozoff, C.M.; Knaff, J.A. Hurricane eyewall replacement cycle thermodynamics and the relict inner eyewall circulation. *Mon. Weather Rev.* **2012**, *140*, 4035–4045. [\[CrossRef\]](#)
48. Battan, J.L. *Radar Observation of the Atmosphere*; University of Chicago Press: Chicago, IL, USA, 1973; 324p.
49. Kossin, J.P.; Eastin, M.D. Two distinct regimes in the kinematic and thermodynamic structure of the hurricane eye and eyewall. *J. Atmos. Sci.* **2001**, *58*, 1079–1090. [\[CrossRef\]](#)
50. Schubert, W.H.; Rozoff, C.M.; Vigh, J.L.; McNoldy, B.D.; Kossin, J.P. On the distribution of subsidence in the hurricane eye. *Q. J. R. Meteorol. Soc.* **2007**, *133*, 595–605. [\[CrossRef\]](#)
51. Schubert, W.H.; Taft, R.K.; Slocum, C.J. Baroclinic effects on the distribution of tropical cyclone eye subsidence. *Front. Earth Sci.* **2022**, *10*, 1062465. [\[CrossRef\]](#)
52. Schubert, W.H.; Montgomery, M.T.; Taft, R.K.; Guinn, T.A.; Fulton, S.R.; Kossin, J.P.; Edwards, J.P. Polygonal eyewalls, asymmetric eye contraction, and potential vorticity mixing in hurricanes. *J. Atmos. Sci.* **1999**, *56*, 1197–1223. [\[CrossRef\]](#)
53. Kossin, J.P.; Schubert, W.H.; Montgomery, M.T. Unstable interactions between a hurricane's primary eyewall and a secondary ring of enhanced vorticity. *J. Atmos. Sci.* **2000**, *57*, 3893–3917. [\[CrossRef\]](#)
54. DeMaria, M. The effect of vertical shear on tropical cyclone intensity change. *J. Atmos. Sci.* **1996**, *53*, 2076–2087. [\[CrossRef\]](#)
55. Corbosiero, K.L.; Molinari, J. The effects of vertical wind shear on the distribution of convection in tropical cyclones. *Mon. Weather Rev.* **2002**, *130*, 2110–2123. [\[CrossRef\]](#)
56. Corbosiero, K.L.; Molinari, J. The relationship between storm motion, vertical wind shear, and convective asymmetries in tropical cyclones. *J. Atmos. Sci.* **2003**, *60*, 366–376. [\[CrossRef\]](#)
57. Molinari, J.; Vollaro, D.; Corbosiero, K.L. Tropical cyclone formation in a sheared environment: A case study. *J. Atmos. Sci.* **2004**, *61*, 2493–2509. [\[CrossRef\]](#)
58. Yang, Y.T.; Kuo, H.C.; Hendricks, E.A.; Peng, M.S. Structural and intensity changes of concentric eyewall typhoons in the western North Pacific basin. *Mon. Weather Rev.* **2013**, *141*, 2632–2648. [\[CrossRef\]](#)
59. Dougherty, E.M.; Molinari, J.; Rogers, R.F.; Zhang, J.A.; Kossin, J.P. Hurricane Bonnie (1998): Maintaining intensity during high vertical wind shear and an eyewall replacement cycle. *Mon. Weather Rev.* **2018**, *146*, 3383–3399. [\[CrossRef\]](#)
60. Hendricks, E.A.; Schubert, W.H.; Taft, R.K.; Wang, H.; Kossin, J.P. Life cycles of hurricane-like vorticity rings. *J. Atmos. Sci.* **2009**, *66*, 705–722. [\[CrossRef\]](#)
61. Kuo, H.C.; Williams, R.T.; Chen, J.H. A possible mechanism for the eye rotation of Typhoon Herb. *J. Atmos. Sci.* **1999**, *56*, 1659–1673. [\[CrossRef\]](#)
62. Oda, M.; Itano, T.; Naito, G.; Nakanishi, M.; Tomine, K. Destabilization of the symmetric vortex and formation of the elliptical eye of Typhoon Herb. *J. Atmos. Sci.* **2005**, *62*, 2965–2976. [\[CrossRef\]](#)
63. Lamb, H. *Hydrodynamics*, 6th ed.; Cambridge University Press: Cambridge, UK, 1932; 738p.
64. Shapiro, L.J.; Montgomery, M.T. A three-dimensional balance theory for rapidly rotating vortices. *J. Atmos. Sci.* **1993**, *50*, 3322–3335. [\[CrossRef\]](#)

65. Lai, T.K.; Hendricks, E.A.; Menelaou, K.; Yau, M.K. Roles of barotropic instability across the moat in inner eyewall decay and outer eyewall intensification: Three-dimensional numerical experiments. *J. Atmos. Sci.* **2021**, *78*, 473–496. [\[CrossRef\]](#)
66. Lai, T.K.; Hendricks, E.A.; Yau, M.K.; Menelaou, K. Roles of barotropic instability across the moat in inner eyewall decay and outer eyewall intensification: Essential dynamics. *J. Atmos. Sci.* **2021**, *78*, 1411–1428. [\[CrossRef\]](#)
67. Lai, T.K.; Hendricks, E.A.; Yau, M.K. Long-term effect of barotropic instability across the moat in double-eyewall tropical cyclone-like vortices in forced and unforced shallow-water models. *J. Atmos. Sci.* **2021**, *78*, 4103–4126. [\[CrossRef\]](#)
68. Slocum, C.J.; Kossin, J.P.; Taft, R.K.; Schubert, W.H. Poster: Instability between the concentric eyewalls of Hurricane Maria (2017). In Proceedings of the 33rd AMS Conference on Hurricanes and Tropical Meteorology, Ponte Vedra, FL, USA, 17 April 2018. Available online: <https://ams.confex.com/ams/33HURRICANE/webprogram/Paper340576.html> (7 January 2023).
69. Taft, R.K.; Schubert, W.H.; Slocum, C.J. Poster: Barotropic instability of axisymmetric double-ring vortices. In Proceedings of the AMS 100th Annual Meeting, Boston, MA, USA, 15 January 2020. Available online: <https://ams.confex.com/ams/2020Annual/meetingapp.cgi/Paper/362737> (7 January 2023).
70. Rostami, M.; Zeitlin, V. Evolution of double-eye wall hurricanes and emergence of complex tripolar end states in moist-convective rotating shallow water model. *Phys. Fluids* **2022**, *34*, 066602. [\[CrossRef\]](#)
71. Arakawa, A. Computational design for long-term numerical integration of the equations of fluid motion: Two-dimensional incompressible flow. Part I. *J. Comput. Phys.* **1966**, *1*, 119–143. [\[CrossRef\]](#)
72. Arakawa, A. Numerical simulation of large-scale atmospheric motions. In *SIAM-AMS Proceedings: Numerical Solution of Field Problems in Continuum Physics*; Birkoff, G., Varga, R. S., Eds.; Am. Math. Soc.: Providence, RI, USA, 1970; Volume 2, pp. 24–40.
73. Adams, L.M.; LeVeque, R.J.; Young, D.M. Analysis of the SOR iteration for the 9-point Laplacian. *SIAM J. Numer. Anal.* **1988**, *25*, 1156–1180. [\[CrossRef\]](#)
74. Adams, J.C. MUDPACK-2: Multigrid software for approximating elliptic partial differential equations on uniform grids with any resolution. *Appl. Math. Comp.* **1993**, *53*, 235–249. [\[CrossRef\]](#)
75. Carton, X.J.; Flierl, G.R.; Polvani, L.M. The generation of tripoles from unstable axisymmetric isolated vortex structures. *Europhys. Lett.* **1989**, *9*, 339–344. [\[CrossRef\]](#)
76. Polvani, L.M.; Carton, X.J. The tripole: A new coherent vortex structure of incompressible two-dimensional flows. *Geophys. Astrophys. Fluid Dyn.* **1990**, *51*, 87–102. [\[CrossRef\]](#)
77. Kloosterziel, R.C.; van Heijst, G.J.F. An experimental study of unstable barotropic vortices in a rotating fluid. *J. Fluid Mech.* **1991**, *223*, 1–24. [\[CrossRef\]](#)
78. Orlandi, P.; van Heijst, G.F. Numerical simulation of tripolar vortices in 2D flow. *Fluid Dyn. Res.* **1992**, *9*, 179–206. [\[CrossRef\]](#)
79. Morel, Y.G.; Carton, X.J. Multipolar vortices in two-dimensional incompressible flows. *J. Fluid Mech.* **1994**, *267*, 23–51. [\[CrossRef\]](#)
80. Carton, X.; Legras, B. The life-cycle of tripoles in two-dimensional incompressible flows. *J. Fluid Mech.* **1994**, *267*, 53–82. [\[CrossRef\]](#)
81. Crowdy, D. A class of exact multipolar vortices. *Phys. Fluids* **1999**, *11*, 2556–2564. [\[CrossRef\]](#)
82. Kloosterziel, R.C.; Carnevale, G.F. On the evolution and saturation of instabilities of two-dimensional isolated circular vortices. *J. Fluid Mech.* **1999**, *388*, 217–257. [\[CrossRef\]](#)
83. Kizner, Z.; Khvoles, R. The tripole vortex: Experimental evidence and explicit solutions. *Phys. Rev. E* **2004**, *70*, 016307. [\[CrossRef\]](#)
84. Rozoff, C.M.; Kossin, J.P.; Schubert, W.H.; Mulero, P.J. Internal control of hurricane intensity variability: The dual nature of potential vorticity mixing. *J. Atmos. Sci.* **2009**, *66*, 133–147. [\[CrossRef\]](#)
85. Ooyama, K. Numerical simulation of the life cycle of tropical cyclones. *J. Atmos. Sci.* **1969**, *26*, 3–40. [\[CrossRef\]](#)
86. Maclay, K.S.; DeMaria, M.; Haar, T.H.V. Tropical cyclone inner-core kinetic energy evolution. *Mon. Weather Rev.* **2008**, *136*, 4882–4898. [\[CrossRef\]](#)
87. Menelaou, K.; Schecter, D.A.; Yau, M.K. On the relative contribution of inertia-gravity wave radiation to asymmetric instabilities in tropical cyclone-like vortices. *J. Atmos. Sci.* **2016**, *73*, 3345–3370. [\[CrossRef\]](#)
88. Menelaou, K.; Yau, M.K. Spontaneous emission of spiral inertia-gravity waves and formation of elliptical eyewalls in tropical cyclone-like vortices: Three-dimensional nonlinear simulations. *J. Atmos. Sci.* **2018**, *75*, 2635–2658. [\[CrossRef\]](#)
89. Hoose, H.M.; Colón, J.A. Some aspects of the radar structure of Hurricane Beulah on September 9, 1967. *Mon. Weather Rev.* **1970**, *98*, 529–533. [\[CrossRef\]](#)
90. Combet, C.; Mouche, A.; Knaff, J.; Zhao, Y.; Zhao, Y.; Vinour, L.; Quilfen, Y.; Chapron, B. Extensive high-resolution synthetic aperture radar (SAR) data analysis of tropical cyclones: Comparisons with SFMR flights and best track. *Mon. Weather Rev.* **2020**, *148*, 4545–4563. [\[CrossRef\]](#)
91. Jackson, C.R.; Ruff, T.W.; Knaff, J.A.; Mouche, A.; Sampson, C.R. Chasing cyclones from space. *Eos* **2021**, *102*. [\[CrossRef\]](#)
92. Carnevale, G.F.; Shepherd, T.G. On the interpretation of Andrews’ theorem. *Geophys. Astrophys. Fluid Dyn.* **1990**, *51*, 1–17. [\[CrossRef\]](#)
93. Shepherd, T.G. Nonlinear stability and the saturation of instabilities to axisymmetric vortices. *Eur. J. Mech. B Fluids* **1991**, *10*, 93–98.
94. Vallis, G.K. *Atmospheric and Oceanic Fluid Dynamics: Fundamentals and Large-Scale Circulation*, 2nd ed.; Cambridge University Press: Cambridge, UK, 2017; 946p. [\[CrossRef\]](#)

95. Martinez, J.; Bell, M.M.; Rogers, R.F.; Doyle, J.D. Axisymmetric potential vorticity evolution of Hurricane Patricia (2015). *J. Atmos. Sci.* **2019**, *76*, 2043–2063. [\[CrossRef\]](#)
96. Orszag, S. Numerical simulation of incompressible flows within simple boundaries: Accuracy. *J. Fluid Mech.* **1971**, *49*, 75–112. [\[CrossRef\]](#)

Disclaimer/Publisher’s Note: The statements, opinions and data contained in all publications are solely those of the individual author(s) and contributor(s) and not of MDPI and/or the editor(s). MDPI and/or the editor(s) disclaim responsibility for any injury to people or property resulting from any ideas, methods, instructions or products referred to in the content.